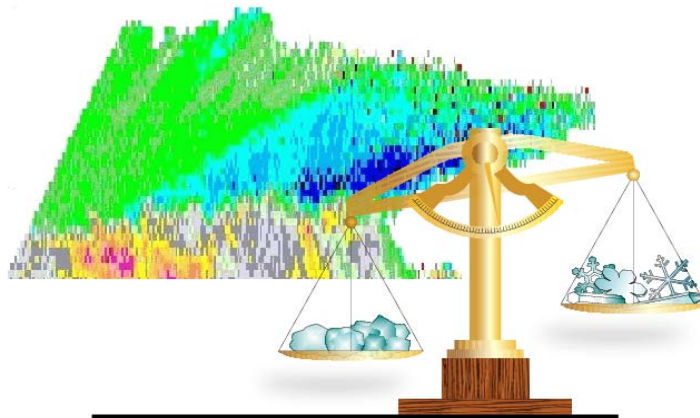# Recombination of super resolution data and ground clutter recognition on the polarimetric WSR-88D

August 2008

*Valery M. Melnikov, Pengfei Zhang, Dusan S. Zrnic, and Alexander Ryzhkov*

**Preamble**


       This report is an augmentation to the "Processing to obtain polarimetric variables on the ORDA" report. It consists of two parts. The first part is titled "Super resolution in dual polarization mode for the WSR-88D". The second part is "Clutter recognition using polarimetric spectral analysis". The primary contributor to the first part is Pengfei Zhang with substantial input from Valery Melnikov and inputs from Dusan Zrnic and Alexander Ryzhkov. The second part reflects the work of Valery Melnikov with substantial contributions by Dusan Zrnic.

       In the first part presented is a functional description of how to recombine super resolution (0.5 deg) polarimetric level II data into regular (legacy 1 deg) resolution. Then test of classification algorithm on these data is made. Test of the classification algorithm demonstrates that it is essentially not affected by the recombination procedure. This is because there is no substantial difference between polarimetric data computed in the super resolution and legacy modes. Nonetheless, testing was done on one data set hence it is premature to accept this finding in general. Additional testing should be made on a variety of weather radar data.

       In "Clutter recognition using polarimetric spectral analysis" we demonstrate that it is possible to recognize clutter at a single range location by examining spectral densities of polarimetric variables. Some additional testing of this technique should be done. Eventually elements of this clutter recognition should be combined with the non polarimetric clutter recognition to produce a very robust algorithm.

       Minor corrections might be needed in this report. These we will make as errors are discovered, and to keep track of the latest version the title includes the month and year when the latest correction has been made.

**TABLE OF CONTENTS**

# I

# SUPER RESOLUTION IN DUAL POLARIZATION MODE FOR THE WSR-88D

Pengfei Zhang, Valery Melnikov, Dusan Zrnic, and Alexander Ryzhkov

### I.1. Introduction

This section contains functional description of computations for recombining super resolution dual polarization data into "legacy" (1 degree) resolution data. Because the recombination will be done on spectral moment data, it is natural to recombine the polarimetric data in the same manner for processing by the algorithms on the RPG and recording. The Open Radar Data Acquisition (ORDA) will produce the following polarimetric variables: reflectivity factor at horizontal polarization $Z_h$, differential reflectivity $Z_{DR}$, cross-correlation coefficient $\rho_{hv}$, and differential phase $\Phi_{DP}$. The reflectivity factor will be computed from the power at horizontal polarization after subtracting the receiver noise power. Similarly, the differential reflectivity and cross-correlation will be computed from the powers after elimination of the noise contribution. Thus these quantities will not be biased by noise. We are using these unbiased variables in the functional description herein.

**Inputs (at super resolution):**

| | |
|---|---|
| $Z(i, j)$: | Censored and quantized reflectivity at gate $i$ and beam $j$ in dBZ; |
| $Z_{dr}(i, j)$: | Censored and quantized differential reflectivity at gate $i$ and beam $j$ in dB; |
| $\rho_{hv}(i, j)$: | Censored and quantized correlation coefficient at gate $i$ and beam $j$; |
| $\phi_{dp}(i, j)$: | Censored and quantized differential phase at gate $i$ and beam $j$ in degree; |
| $N_h$: | Noise power in the horizontal channel in internal processor unit; |
| $N_v$: | Noise power in the vertical channel in internal processor unit; |
| $Att$: | Atmospheric attenuation factor in dB/km; |
| $C$: | Radar constant in dB. |

**Outputs (at legacy resolution):**

| | |
|---|---|
| $Z_c(i,jc)$: | Quantized and recombined reflectivity at gate $i$ and beam $jc$; |
| $Z_{drc}(i,jc)$: | Quantized and recombined differential reflectivity at gate $i$ and beam $jc$; |
| $\rho_{hvc}(i,jc)$: | Quantized and recombined correlation coefficient at gate $i$ and beam $jc$; |
| $\phi_{dpc}(i,jc)$: | Quantized and recombined differential phase at gate $i$ and beam $jc$. |

### I.2 Procedures

Herein we present the functional description of the recombination procedure. **Note:** If $\phi_{dp}$ is folded at super resolution, unfolding $\phi_{dp}$ is needed before the recalculation of complex covariance.

1) Recalculate powers $P_h(i, j)$ and $P_v(i, j)$, signal-to-noise ratios $snr_h$ and $snr_v$ in horizontal ($h$) and vertical ($v$) channels, and complex covariance $reR_{hv}(i, j)$ and $imR_{hv}(i, j)$ from dual polarization level II data at super resolution.

$$snr_h(i, j) = 10^{0.1(Z(i,j) - C + Att*R - 20\log R)} , \qquad (1)$$

$$P_h(i, j) = N_h * snr_h(i, j), \qquad (2)$$

$$P_v(i, j) = \frac{P_h(i, j)}{10^{0.1Z_{dr}(i,j)}} , \qquad (3)$$

$$snr_v(i, j) = P_v(i, j)/N_v , \qquad (4)$$

$$reR_{hv}(i, j) = \rho_{hv}(i, j)[P_h(i, j)P_v(i, j)]^{1/2} \cos(-\phi_{dp}(i, j) * \pi/180) , \text{ and} \qquad (5)$$

$$imR_{hv}(i, j) = \rho_{hv}(i, j)[P_h(i, j)P_v(i, j)]^{1/2} \sin(-\phi_{dp}(i, j) * \pi/180) , \qquad (6)$$

2) Recombine them back at $1^{\circ}$ beamwidth

$$P_{hc}(i, jc) = 0.5 * (P_h(i, j) + P_h(i, j+1)), \qquad (7)$$

$$P_{vc}(i, jc) = 0.5 * (P_v(i, j) + P_v(i, j+1)), \qquad (8)$$

$$reR_{hvc}(i, jc) = \frac{reR_{hv}(i, j) + reR_{hv}(i, j+1)}{2} , \text{ and} \qquad (9)$$

$$imR_{hvc}(i, jc) = \frac{imR_{hv}(i, j) + imR_{hv}(i, j+1)}{2} , \qquad (10)$$

where $jc$ is the index for recombined beams.

**Note:** Rules for recombination of missing data with valid data:
For powers in horizontal channel:
  According to "Super Resolution Base Data Recombination Algorithm", a non-zero value PBG is given as
$$PBG = 10^{0.1*(10\log_{10}(0.7) + 10\log_{10}(Nh) + THZ)} ,$$
  where THZ is the censoring threshold for reflectivity.

  a) If both $P_h(i, j)$ and $P_h(i, j+1)$ are missing, then $P_{hcz}(i, jc)$ is set to be missing.
  b) If $P_h(i, j)$ or $P_h(i, j+1)$ is missing, then

$$P_{hcz}(i, jc)=0.5*(PBG+P_h(i, j+1)),$$
$$\text{or } P_{hcz}(i, jc)=0.5*(P_h(i, j)+PBG),$$

where recombined power $P_{hcz}$ in horizontal channel is for the calculation of recombined reflectivity only.

For dual-polarization variables, the rules are
  a) If $P_h(i, j)$ is missing and $P_h(i, j+1)$ is valid, then $P_{hc}(i, jc)$ is equal to $P_h(i, j+1)$;
  b) If $P_h(i, j)$ is valid and $P_h(i, j+1)$ is missing, then $P_{hc}(i, jc)$ is equal to $P_h(i, j)$;
  c) If $P_v(i, j)$ is missing and $P_v(i, j+1)$ is valid, then $P_{vc}(i, jc)$ is equal to $P_v(i, j+1)$;
  d) If $P_v(i, j)$ is valid and $P_v(i, j+1)$ is missing, then $P_{vc}(i, jc)$ is equal to $P_v(i, j)$.

The rules for real and imaginary parts of correlation function are:
  a) If $reR_{hv}(i, j)$ is missing and $reR_{hv}(i, j+1)$ is valid, then $reR_{hvc}(i, jc)$ is equal to $reR_{hv}(i, j+1)$;
  b) If $reR_{hv}(i, j)$ is valid and $reR_{hv}(i, j+1)$ is missing, then $reR_{hvc}(i, jc)$ is equal to $reR_{hv}(i, j)$;
  c) If $imR_{hv}(i, j)$ is missing and $imR_{hv}(i, j+1)$ is valid, then $imR_{hvc}(i, jc)$ is equal to $imR_{hv}(i, j+1)$;
  d) If $imR_{hv}(i, j)$ is valid and $imR_{hv}(i, j+1)$ is missing, then $imR_{hvc}(i, jc)$ is equal to $imR_{hv}(i, j)$.

Time series data (in phase I, and quadrature phase Q) were obtained with the KOUN radar as a large mesoscale convective system was passing by the radar site on June, 29, 2007. This versatile data contains echoes in clear air (from insects), stratiform precipitation, and convective comprised of few growing cells, few decaying, and an active squall line.
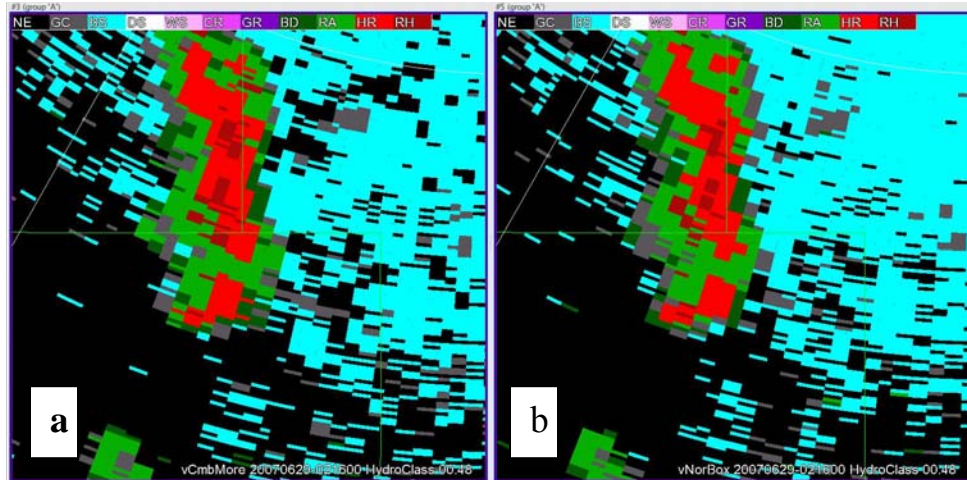


Fig.1. Classification fields based on (a) recombined data and (b) legacy resolution data.

Classification field generated by using all the radar variables is the best to show the results of recombination. It is displayed in Fig. 1 with classification based on legacy resolution data. As expected, the main feature in the classified field of the recombined

data does not show significant difference from the one of the legacy data. Thus in this case the recombination procedure has a negligible effect on the classification results.

3) Recalculation of radar variables:

Calculate recombined Signal-to-Noise Ratio $SNR_{hc}$ and $SNR_{vc}$ in dB as follows:

$$SNR_{hc}(i, jc) = 10log(P_{hc}(i, jc)/N_h), \tag{11}$$
$$SNR_{vc}(i, jc) = 10log(P_{vc}(i, jc)/N_v). \tag{12}$$

$$Z_c(i, jc) = C + 20log(R(i)) + SNR_{hc}(i, jc). \tag{13}$$

Note:
  Recombined differential reflectivity $Z_{drc}(i, jc)$ will be calculated only if both $P_{hc}(i, jc)$ and $P_{vc}(i, jc)$ are not missing, otherwise these variables are set to be missing. Recombined correlation coefficient $\rho_{hvc}(i, jc)$ will be calculated only if $P_{hc}(i, jc)$, $P_{vc}(i, jc)$, $reR_{hvc}(i, jc)$, and $imR_{hvc}(i, jc)$ are not missing, otherwise these variables are set to be missing.
  Recombined differential phase $\phi_{dpc}(i, jc)$ will be calculated only if both $reR_{hvc}(i, jc)$ and $imR_{hvc}(i, jc)$ are not missing, otherwise these variables are set to be missing.

Recombined differential reflectivity $Z_{drc}$ can be obtained as follows:

$$Z_{drc}(i, jc) = 10log\left(\frac{P_{hc}(i, jc)}{P_{vc}(i, jc)}\right). \tag{14}$$

  Then recombined correlation coefficient $\rho_{hvc}$ and differential phase $\phi_{dpc}$ are calculated based on the followed equations:

$$\rho_{hvc}(i, jc) = \frac{[reR_{hvc}^2(i, jc) + imR_{hvc}^2(i, jc)]^{1/2}}{[(P_{hc}(i, jc)P_{vc}(i, jc))]^{1/2}} \tag{15}$$

$$\phi_{dpc}(i, jc) = -\frac{180}{\pi} * tan^{-1}[\frac{imR_{hvc}(i, jc)}{reR_{hvc}(i, jc)}] \tag{16}$$

Notes: Rules for missing data:
  a)  If $P_{hc}(i, jc)$ or $P_{vc}(i, jc)$ is missing, then $Z_{drc}(i, jc)$ is set to be missing.
  b)  If $reR_{hvc}(i, jc)$ or $imR_{hv}(i, jc)$ is missing, then $\phi_{dpc}(i, jc)$ is set to be missing.
  c)  If one of $reR_{hvc}(i, jc)$, $imR_{hvc}(i, jc)$, $P_{hc}(i, jc)$, and $P_{vc}(i, jc)$ is missing, then $\rho_{hvc}(i, jc)$ is set to be missing.

4) Quantization of recombined variables:
  The quantization of recombined radar variables $V$ is performed based on the following formula:

$$V_{integer} = round(V*scale + offset) \tag{17}$$
$$V_{quantized} = ( V_{integer} - offset)/scale \tag{18}$$

where the values of scale and offset for different radar variables are listed in the Table 1.

Table 1: Values of scale and offset for different radar variables.

| Variables | $Z_c$ | $Z_{drc}$ | $\phi_{dpc}$ | $\rho_{hvc}$ |
|-----------|-------|-----------|--------------|--------------|
| scale | 2.0 | 16.0 | 2.8361 | 300.0 |
| offset | 66.0 | 128.0 | 2.0 | -60.0 |

### I.3. Comparison between recombined variables and variables with legacy resolution

The legacy and super resolution data sets we processed are generated from time series data observed by KOUN at 0216 UTC on 29 June 2007. 17 samples are used to produce the powers in horizontal and vertical channels and complex covariance in both legacy and super resolution mode. Rectangular window is applied to collect legacy resolution data. For super resolution data, von Hann window is used. The azimuthal layout of data collection is shown in Fig.2.

In legacy resolution, pulse #17 coincides with pulse #1 of adjacent radial whereas in super resolution, the centers of adjacent radials are at pulses #5 and #13. This could account for some minor differences in the fields. Fine features (left panel in Fig.3, especially reflectivity) are hard to see in the legacy fields but can be easily recognizede in the super resolution fields (left panel in Fig.3). On the other hand, super resolution fields are noisier than legacy resolution fields.

Following the procedures described in the first section, the recombined variables are calculated. Then they are compared with the variables in legacy resolution. The differences between recombined and legacy resolution variables are estimated at the gate with valid observation. The histograms of the differences ($V_{recombined} - V_{legacy\ resolution}$) of radar variables between recombined and legacy resolution are displayed in Fig.4. Here the letter "V" represents the radar variable. The average differences of the radar variables over the entire tilt at 0.5° elevation angle are shown in Table 2.
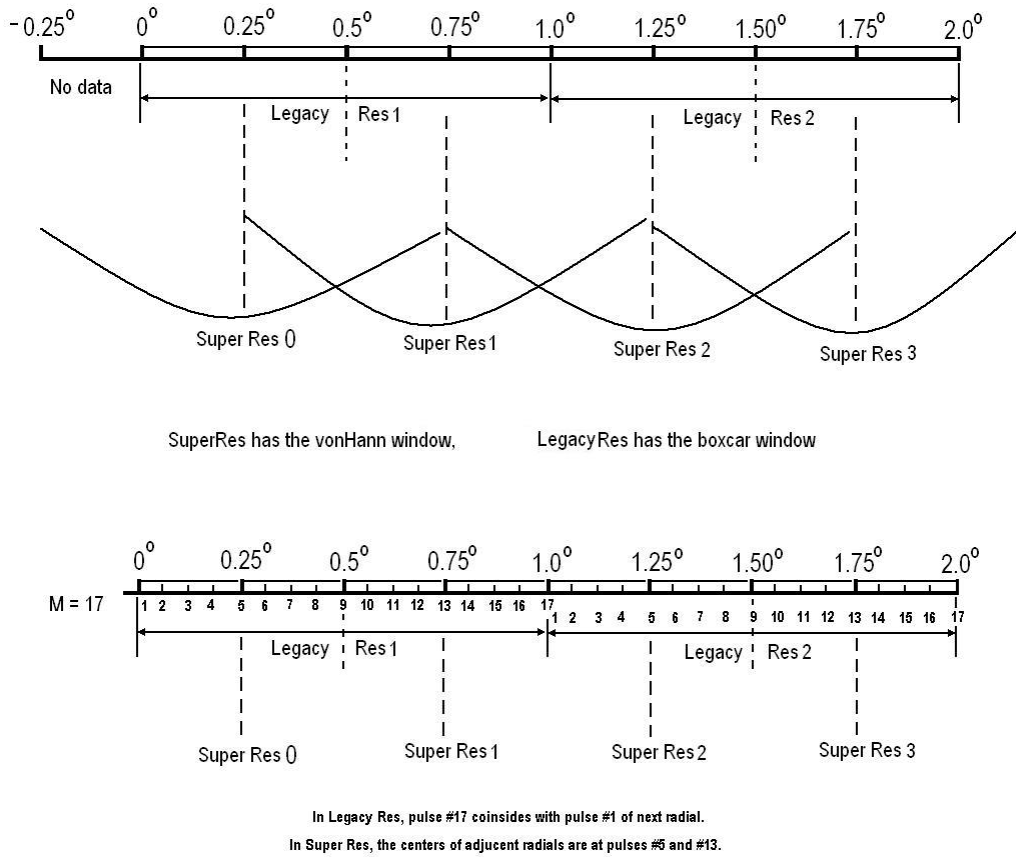
Fig.2. Layout of data processed in Legacy Resolution (NR normal resolution) and Super Resolution (SR) modes. (Upper panel): Azimuthal layout of data collected with the rectangular window in NR and the von Hann window in SR (semi arcs in the figure). Azimuthal layout is shown for azimuth from $0^o$ to $2^o$. (Lower panel): Radar pulse layout for the number of samples M = 17.

Table 2: Average difference ($V_{recombined} - V_{legacy\ resolution}$) for tilt at $0.5^o$ elevation angle.

| Average Differences | Reflectivity (dBZ) | $Z_{dr}$(dB) | $\rho_{hv}$ | $\phi_{dp}$(deg) |
|---|---|---|---|---|
| Over a tilt | -0.024 | -0.044 | 0.0067 | -0.16 |

The recombined reflectivity, differential reflectivity, correlation coefficient, and differential phase are displayed with corresponding variables in legacy resolution in Fig.5. It can be seen that the features in both fields are similar. Combined with results in Fig.4 and Table 2, we conclude that the recombination does not distort or bias the fields.
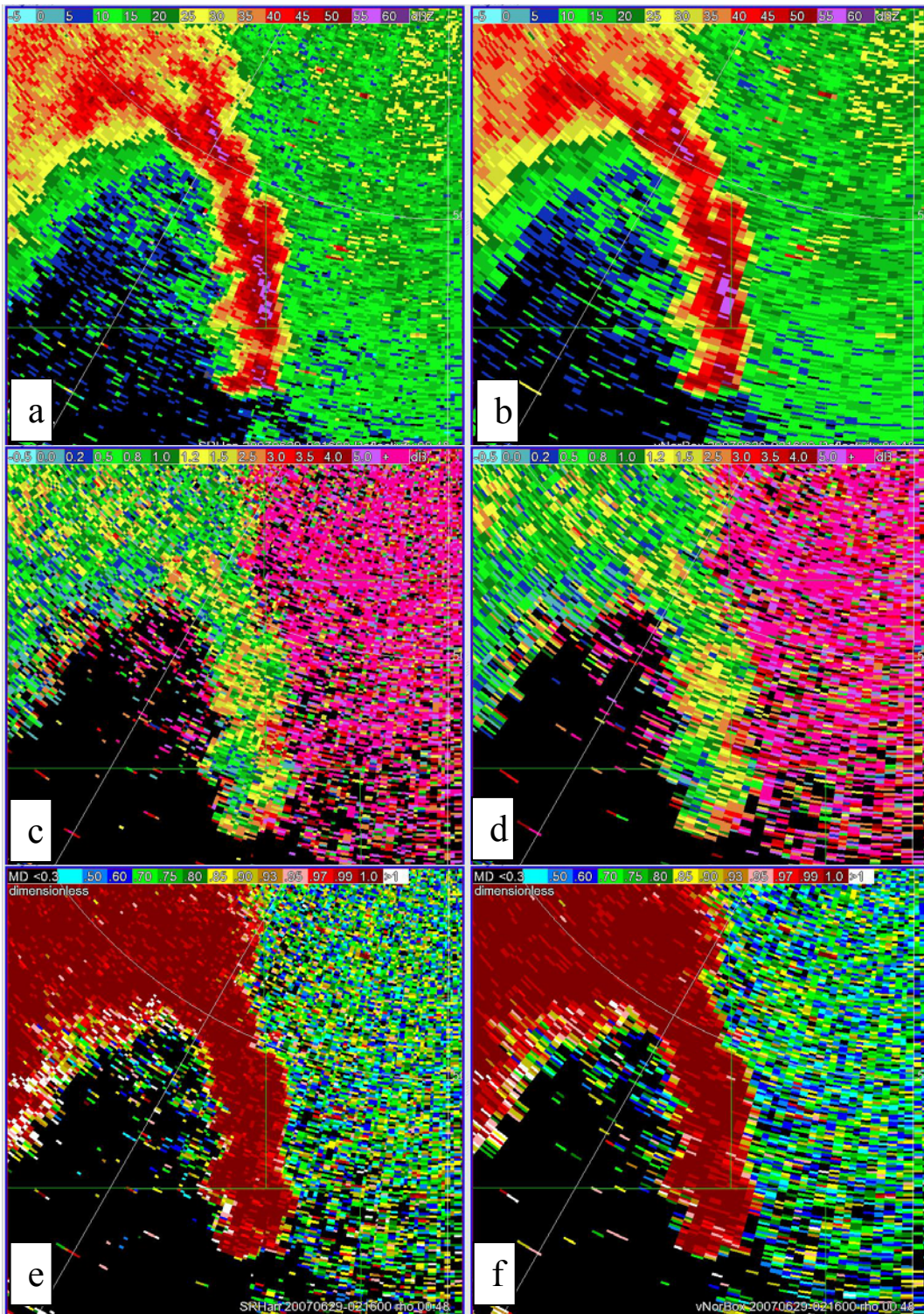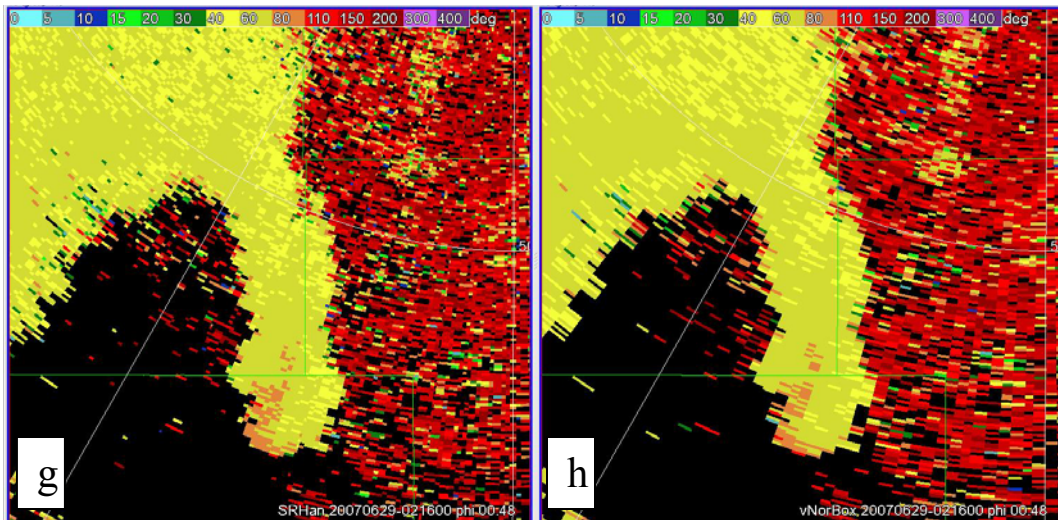
Fig.3. Radar variables in super resolution (left panel) and legacy resolution (right panel). (a) and (b) are reflectivity. (c) and (d) are differential reflectivity. (e) and (f) are correlation coefficient. (g) and (h) are differential phase.
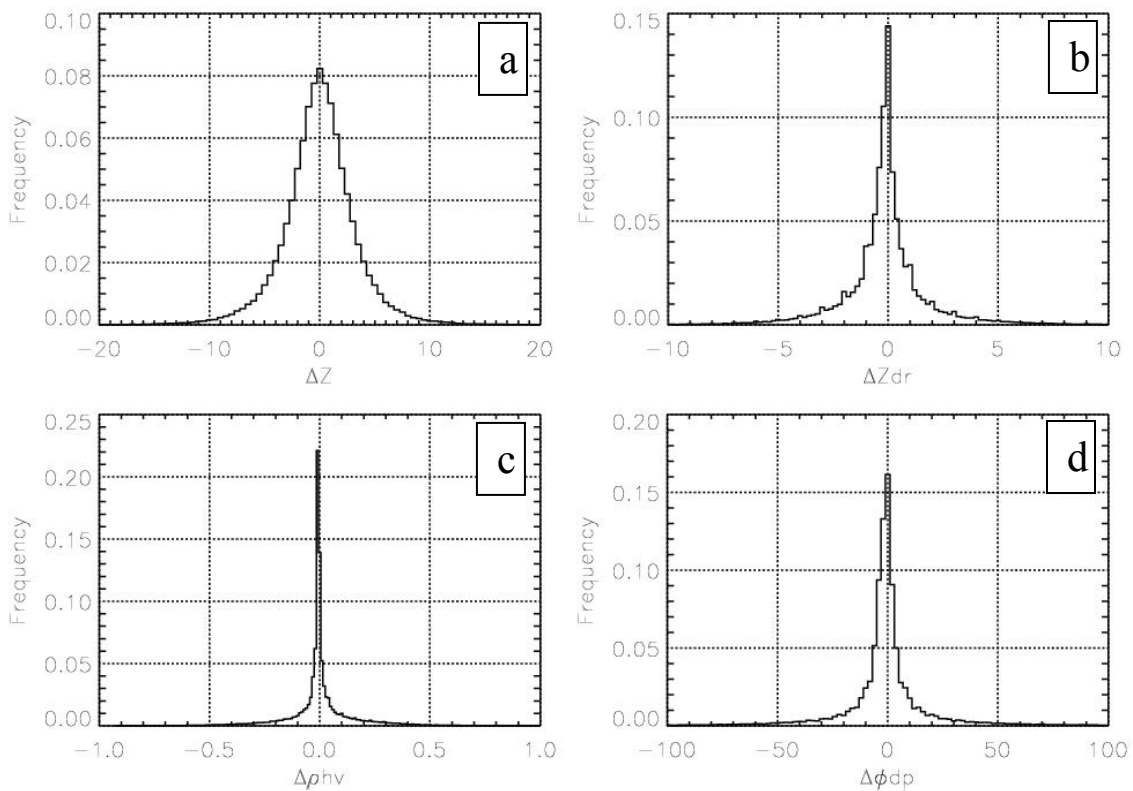


Fig.4. Histograms of differences between recombined and legacy (a) reflectivity, (b) differential reflectivity, (c) correlation coefficient, and (d) differential phase at range locations that have valid observations.
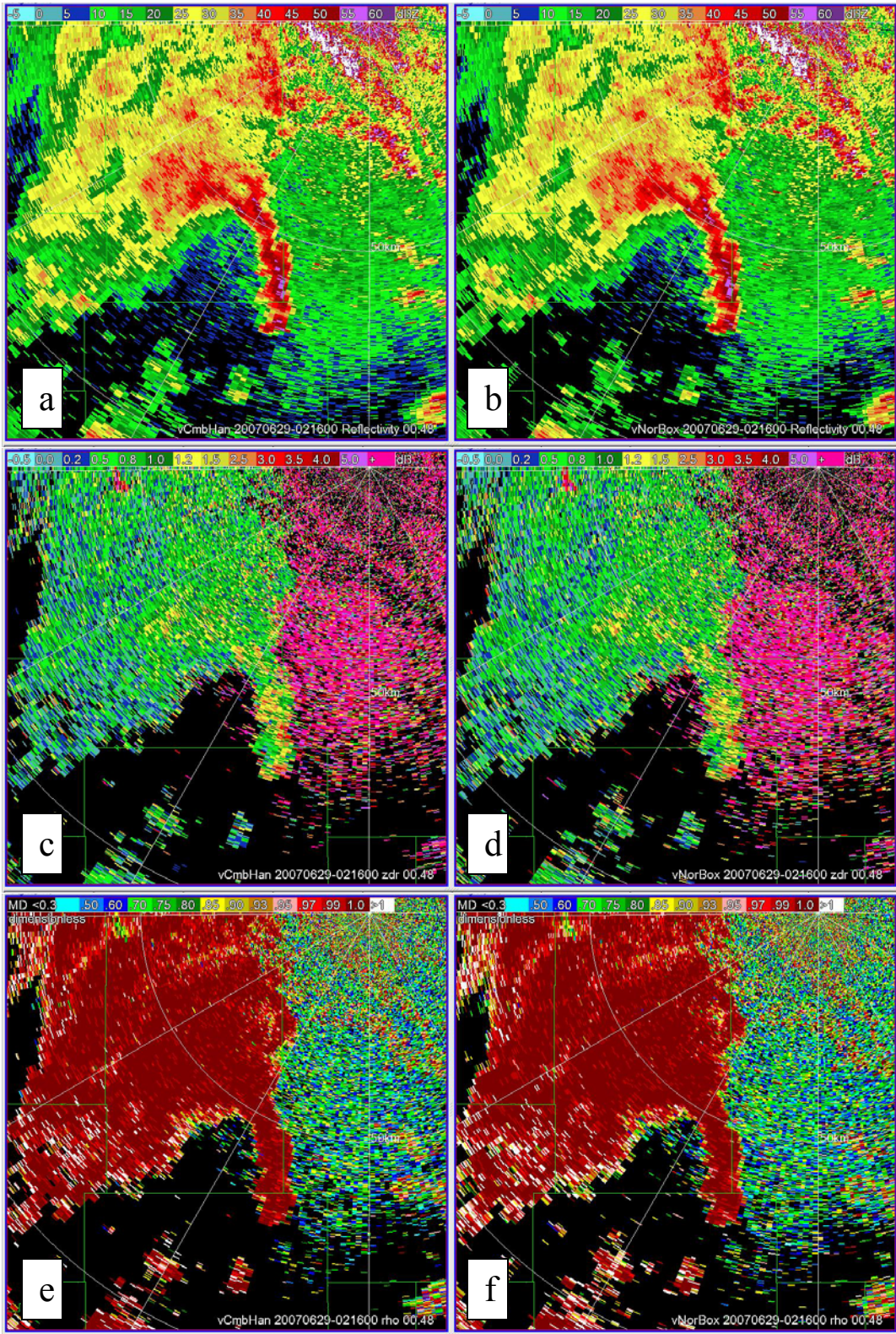
Fig.5. Recombined reflectivity (a), differential reflectivity (c), correlation coefficient (e), and differential phase (f) are on left side. Reflectivity (b), diffe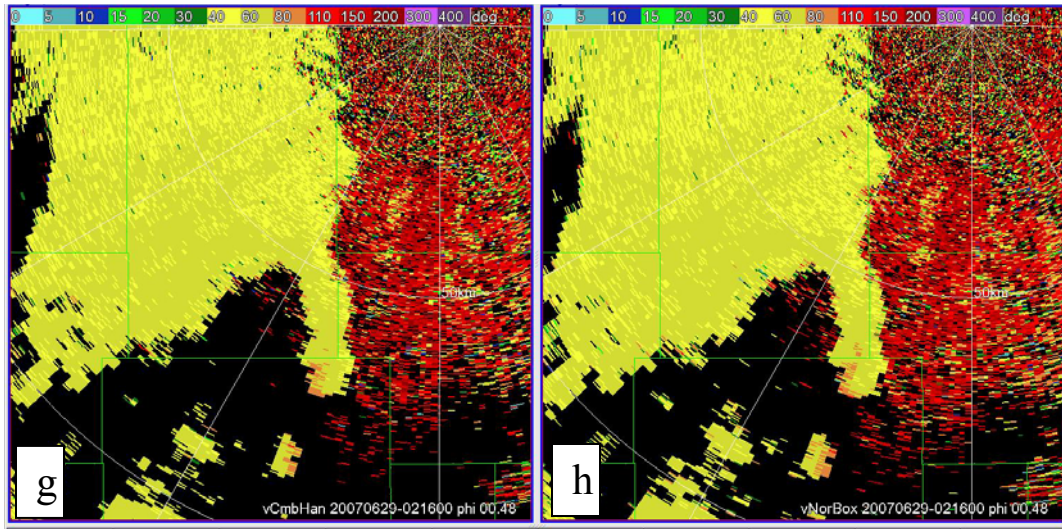rential reflectivity (d), correlation coefficient (f), and differential phase (g) in legacy resolution are on the right side.

# II

# CLUTTER RECOGNITION
# USING POLARIMETRIC SPECTRAL ANALYSIS

Valery Melnikov and Dusan Zrnic

## II.1 Introduction

Ground clutter complicates interpretation of radar variables; hence it is desirable to be filtered out. Several approaches have been explored for such filtering on single-polarization radars: prerecording a power clutter map and then subtracting it from observed data (e.g., Steiner and Smith, 2002; Yo-Han Cho et al., 2006), applying Doppler filters (Siggia and Passarelli, 2004; Ice et al., 2004; Kessinger et al., 2003; Berenguer et al., 2006), and a combination of both as has been implemented on the WSR-88D network in the USA, i.e., a Doppler filter is applied at range gates selected from a prerecorded clutter map. Clutter returns vary over time due to changes of ambient atmosphere, that may cause anomalous propagation and ducting of radio waves; new clutter areas can be formed in rain due to watering of the ground and changes in propagation parameters in rain. This necessitates an adaptive approach for clutter filtering. The Gaussian model adaptive processing, GMAP, for clutter filtering (Siggia and Passarelli, 2004) is a very successful application of such approach. On the WSR-88D network, GMAP is applied according to a fixed (static) clutter map. Herein we describe a procedure that can be used to adaptively generate a dynamic "clutter map".

The US National Weather Service is planning to upgrade the WSR-88D radar network with dual polarization (Saffle et al., 2007). Thus significant new capability including recognition of echoes from ground clutter will become available. Thus far recognition of clutter was based on the values of polarimetric variables (e.g., Zrnic et al., 2001) and their texture, i.e., spatial variations of polarimetric parameters (Dixon et al., 2006, Gourley et al. 2007). These approaches have high accuracy of clutter recognition in areas without rain. Rain decreases the accuracy. Herein we do not consider the textures of polarimetric parameters and focus on clutter recognition in a single range gate. We show that the few Doppler spectral lines around zero velocity can be used to recognize clutter in cases with and without rain. It means that an adaptive clutter filter can be designed for a single range location.

Ground clutter cancellation is most needed at low elevations wherein clutter is strongest. Currently, volume coverage pattern #11, VCP11, is most frequently used on the WSR-88D. Two lowest elevations of VCP11 are at $0.5^{o}$ and $1.45^{o}$. Each tilt consists of the surveillance sweep with the number of samples $M = 17$ and the pulse repetition frequency 320 Hz (PRI=1) followed by the Doppler sweep with PRF of about 1000 Hz (PRI=5) and the number of samples between 48 and 51 depending on the exact PRF. Ground clutter recognition and cancellation must be applied to both sweeps. We present our results for the Doppler scan first and then compare with ones obtained in the surveillance scan.

## II.2. The algorithm

Differential reflectivity, $Z_{DR}$, the differential phase $\varphi_{dp}$, and copolar correlation coefficient $\rho_{hv}$ (Doviak and Zrnic, 2006), are used in the following clutter recognition algorithm. Fig. 1 illustrates differences in polarimetric parameters of ground clutter and weather. The data were obtained with the polarimetric prototype of the WSR-88D, i.e., KOUN, situated in Norman, OK. The clutter data were collected in clear air and weather data were collected at distances beyond 50 km to avoid possible clutter contamination. Visual inspection of the weather data used in Fig. 1 shows that echoes due to anomalous propagation were absent. It is seen from the figure that the variables from clutter have significantly wider distributions than the ones from weather, i.e., the polarimetric variables from clutter frequently lay outside intervals occupied by weather values. Despite of obvious difference in distributions in weather and clutter, there are large areas where weather and clutter overlap. So none of the parameters can be used individually for clutter recognition at a single range location. Averaging over few range locations makes such recognition more satisfactory (e.g., Zrnic et al., 2001). But no spatial averaging is considered herein.
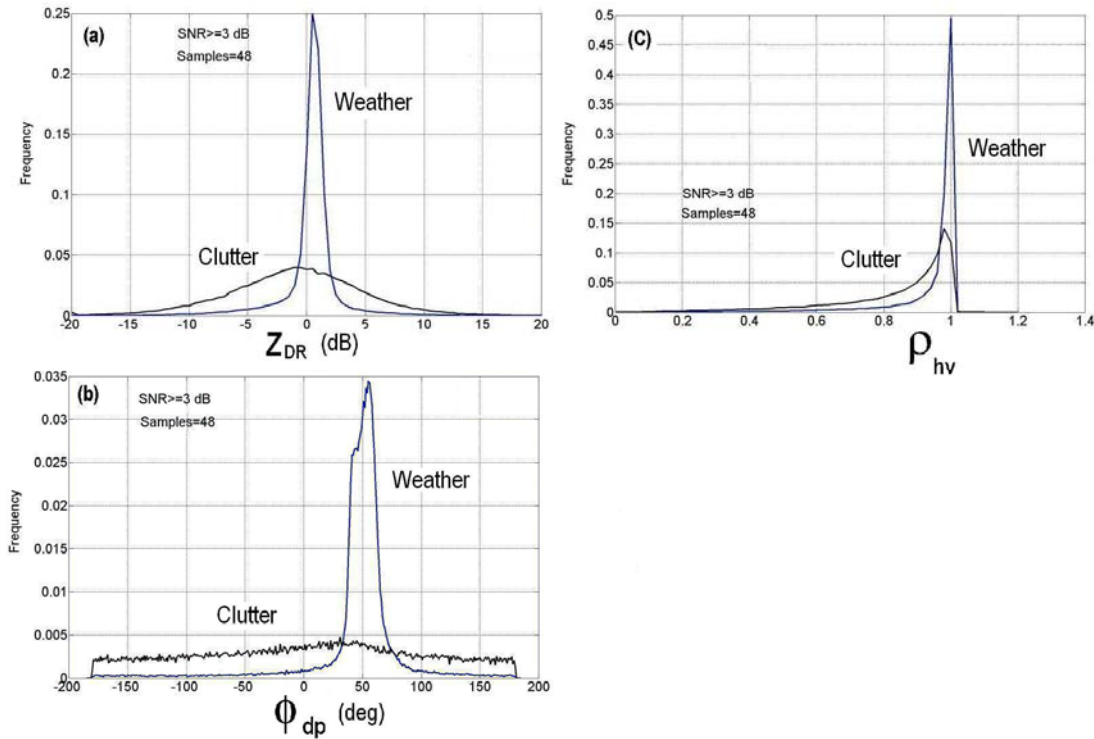


Fig.1. Distributions of polarimetric parameters for weather and clutter. The weather data were collected on June 26, 2007 at 1217 UT and clutter collected on December 19, 2007 at 0136 UT. Elevation is 0.5°. SNR >=3 dB, $M$=48. WSR-88D KOUN.

It is known that the Doppler spectra of clutter returns are narrow (e.g., Beglesley, 2001), i.e., the main spectral lobe occupies few central lines. In contrast to clutter spectra, weather spectra are usually broader and have nonzero mean Doppler velocities. So to recognize clutter, the polarimetric information around the zero frequency Doppler spectral line can be analyzed.

In this report, the polarimetric properties of three central spectral lines have been studied, i.e. the zero frequency line and two lines around the zero one. In the Doppler mode of the WSR-88D, these three lines occupy velocity interval of 2.4 m s$^{-1}$ (velocity unambiguous interval is $\pm$ 27.6 m s$^{-1}$ and the total number of spectral lines is $M=48$). Vast majority of clutter's spectrum widths are in 2.4 m s$^{-1}$ interval so we expect that the three lines represent the whole clutter spectra well. In Fig. 2a, spectra at H- and V-polarizations are shown; the data were collected in snowfall on December 12th, 2006. Fig. 2(b) shows 3-line spectra at both polarizations centered at zero velocity. The residual spectra obtained by subtracting the 3-line spectra from the full spectra is displayed in Fig. 2(c). Four polarimetric variables are calculated using the 3-line spectra: differential reflectivity ($\tilde{Z}_{DR}$), differential phase shift ($\tilde{\varphi}_{dp}$), copolar correlation coefficient ($\tilde{\rho}_{hv}$), and the power ($\tilde{P}_h$). Radar parameters from the full spectrum will be denoted as $Z_{DR}$, $\varphi_{dp}$, $\rho_{hv}$, and $P_h$. The Von Hann spectral window has been applied to the time series data to obtain the spectra.
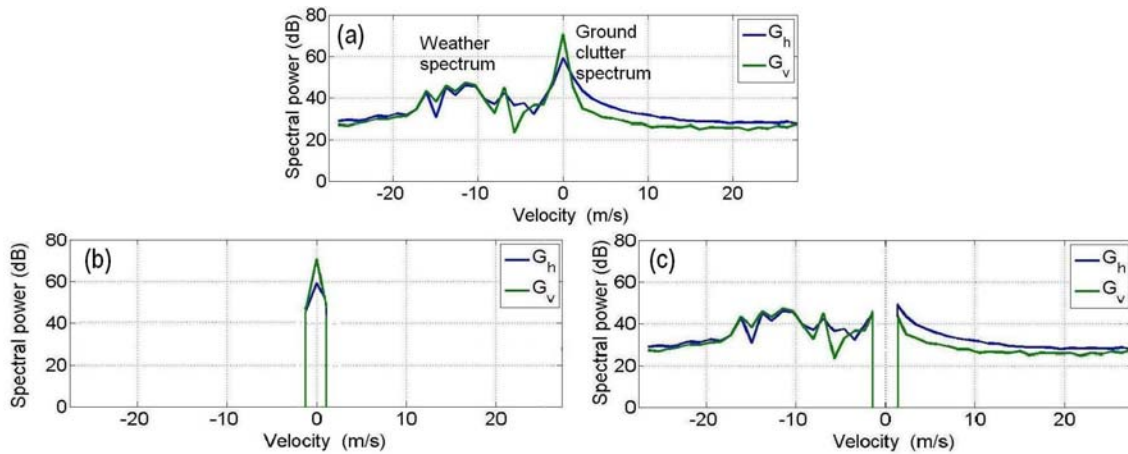


Fig.2. (a): Spectra at H (blue line) and V (green line) polarizations recorded in snowfall on December 12, 2006, 0028:27; azimuth is 133$^\circ$, elevation is 2.5$^\circ$, PRF=1000 Hz, $M=48$. The spectral powers are in the internal processor units. (b): 3-line spectra obtained from the spectra in Fig. 2(a). (c): residual spectra obtained by removing the 3-line spectra shown in Fig. 2(b) from the full spectra in Fig. 2(a).

To recognize ground clutter, the following algorithm is applied at a given range location. The echo is considered as ground clutter if

$$\tilde{Z}_{DR} > \tilde{Z}_{DR2}, \text{ or } \tilde{Z}_{DR} < \tilde{Z}_{DR1} \qquad \text{or} \qquad (1)$$

$$\tilde{\rho}_{hv} \leq \tilde{\rho}_{hv0}, \qquad \qquad \text{or} \qquad (2)$$

$$|\tilde{\varphi}_{dp} - \overline{\varphi}_{dp}| \geq \tilde{\varphi}_{dp0}, \qquad (3)$$

and

$$\tilde{SNR}_h \geq \tilde{SNR}_{h0}, \qquad (4)$$

where $\tilde{Z}_{DR1}, \tilde{Z}_{DR2}, \tilde{\varphi}_{dp0}, \tilde{\rho}_{hv0}$ are predetermined thresholds, and $\tilde{SNR}_{h0}$ is the SNR threshold which is imposed to avoid contamination from noise. Note that the thresholds are imposed on the 3-line spectrum not to the full spectrum. It means that signals with spectral component sufficiently far from zero velocity are not included in the analysis. This is sketched in Fig. 3. The full weather spectrum G($v$) has strong total power with its peak located away from zero velocity. The three spectrum amplitudes G$_{-1}$, G$_0$, and G$_1$ constitute $\tilde{P} = $ G$_{-1}$ + G$_0$ + G$_1$ power. G$_0$ is the amplitude of the spectral line at zero Doppler velocity. $\tilde{SNR}$ is calculated as:

$$\tilde{SNR} \geq \frac{\tilde{P} - 3N/M}{3N/M}, \qquad (5)$$

where $N$ is the noise power in the channel. The mean noise power at one spectral line is $N/M$, so the noise power at three spectral lines is $3N/M$. $\tilde{SNR}$ is calculated for the H- and V-channels using their mean noise powers.

The polarimetric parameters for the 3-line spectrum are calculated as follows. Differential reflectivity is

$$\tilde{Z}_{DR} = \frac{\tilde{P}_h - 3N_h/M}{\tilde{P}_v - 3N_v/M}. \qquad (6)$$

The differential phase and copolar correlation coefficient are calculated in frequency domain using the complex spectral coefficients g$_{-1}$, g$_0$, and g$_1$ of the three complex spectral coefficients in the polarimetric channels (G$_n$ = |g$_n$|$^2$):

$$\tilde{\varphi}_{dp} = \arg(g_{-1(h)}g^*_{-1(v)} + g_{0(h)}g^*_{0(v)} + g_{1(h)}g^*_{1(v)}). \qquad (7)$$

$$\tilde{\rho}_{hv} = \frac{|g_{-1(h)}g^*_{-1(v)} + g_{0(h)}g^*_{0(v)} + g_{1(h)}g^*_{1(v)}|}{[(\tilde{P}_h - 3N_h/M)(\tilde{P}_v - 3N_v/M)]^{1/2}}. \qquad (8)$$

$$\tilde{P}_h = g_{-1(h)}g^*_{-1(h)} + g_{0(h)}g^*_{0(h)} + g_{1(h)}g^*_{1(h)} = G_{-1(h)} + G_{0(h)} + G_{1(h)}, \qquad (9a)$$

$$\widetilde{P}_v = g_{-1(v)}g^*_{-1(v)} + g_{0(v)}g^*_{0(v)} + g_{1(v)}g^*_{1(v)} = G_{-1(v)} + G_{0(v)} + G_{1(v)}, \tag{9b}$$
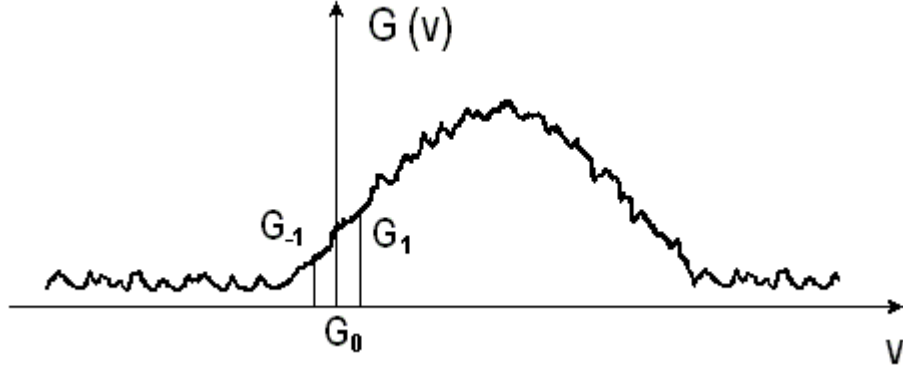
where the asterisk denotes complex conjugate.



Fig.3. Sketch of a weather velocity spectrum with zero velocity line $G_0$ and two nearest lines $G_{-1}$ and $G_1$.

Observations on the WSR-88D KOUN show that weather $Z_{DR}$ lay in the interval -2 to 5 dB (most frequently, -1 to 4 dB). So -2 dB is selected as $\widetilde{Z}_{DR1}$ and 5 dB is selected as $\widetilde{Z}_{DR2}$. Negative $Z_{DR}$ is frequently observed at the tops of severe thunderstorms where strong electric fields align cloud crystals vertically. This effect can be neglected in ground clutter recognition because only lowest elevation angles are considered. Negative $Z_{DR}$ can also be caused by strong differential attenuation. To mitigate this effect, we suggest applying a correction of differential reflectivity using measured specific differential phase before the clutter recognition. Presently the algorithm makes no such correction on $Z_{DR}$, thus the interval $\widetilde{Z}_{DR1}$ to $\widetilde{Z}_{DR2}$ is rather large. $Z_{DR}$ of 5 dB and higher can be measured in the presence of insects and birds so for weather echoes, 5 dB was chosen for upper $Z_{DR}$ threshold.

Threshold $\widetilde{\rho}_{hv0}$ for weather was set to 0.8. Weather signals have the correlation coefficient larger than this threshold. However in the bright band, $\rho_{hv}$ can occasionally drop to 0.8 and this can affect the algorithm when the melting layer is very close to the ground. Data analysis might be needed to deal with such situations.

Eq. (3) sets a threshold for the differential phase. Note that in Fig. 1(b) the differential phases are plotted with the system phase that should be subtracted in differential phase measurements. Eq. (3) expresses a limitation on phase fluctuations so the threshold $\widetilde{\varphi}_{dp0}$ can be obtained from the standard deviation, SD, of differential phases (Melnikov and Zrnic, 2007):

$$SD(\varphi_{dp}) = \frac{180}{\pi (2M)^{1/2} \rho_{hv}} \left( \frac{SNR_h + SNR_v + 1}{SNR_h \, SNR_v} + \frac{1 - \rho_{hv}^2}{\pi^{1/2} \sigma_{vn}} \right)^{1/2} \text{ (deg)}, \qquad (10)$$

where $\sigma_{vn}$ is the normalized spectrum width, i.e., a ratio of the spectrum width and unambiguous Doppler velocity: $\sigma_{vn} = \sigma_v / v_u$. Using threshold $\tilde{\rho}_{hv0} = 0.8$, $\widetilde{SNR}_{h0} = 3$ dB, $M = 48$, $\sigma_v = 1$ m s$^{-1}$, we get SD = 19°. The distribution of $\varphi_{dp} - \overline{\varphi}_{dp}$ is nearly symmetrical so we use $\tilde{\varphi}_{dp0} \approx$ SD = 20°. Weather $\rho_{hv}$ is usually greater than 0.95 therefore most of $|\varphi_{dp} - \overline{\varphi}_{dp}|$ will be smaller than 20°.

For weather echoes, $\tilde{Z}_{DR}$, $\tilde{\rho}_{hv}$ or $\tilde{\varphi}_{dp}$ can be recognized as "clutter" due to natural signal fluctuation. So the algorithm should also be characterized with the false alarm rate for true weather echoes. Probability of such occurrences increases with the decrease of $\widetilde{SNR}$. It is shown in the Appendix that if the weather power exceeds the clutter power by 30 dB or more, the clutter contribution to the polarimetric moments can be neglected, the echo can be considered as "weather like" and there is no need for the algorithm's application. This can save processing time. For now, the algorithm is applied "off line" and does not include this option.

All the algorithm's thresholds are summarized in Table 1 and the radar parameters are in Table 2.

Table 1. Threshold parameters used in clutter recognition

| $\widetilde{SNR}_{h0}$, dB | $\tilde{Z}_{DR1} / \tilde{Z}_{DR2}$, dB | $\tilde{\rho}_{hv0}$ | $\tilde{\varphi}_{dp0}$, deg |
|---|---|---|---|
| 3 | -2 / 5 | 0.8 | 20 |

Table 2. Radar parameters used in  data collection

| Elevation, deg | Antenna rate, deg/s | Number of samples | Azimuthal resolution, deg | Pulse repetition frequency, Hz |
|---|---|---|---|---|
| 0.5 | 20 | 48 | 1 | 1013 |

### II.3. Results
*a) Ground clutter and insects*
To justify the thresholds used in clutter recognition (Table 1), data were collected in clear air. Clear air returns are different for warm and cold seasons as demonstrated in Fig. 4. The right panel of the figure exhibits more echo due to insects. The insects' echoes have significant SNR at close distance so they pass criterion (4) and are analyzed by the algorithm (1)-(3).

Distributions of the polarimetric parameters for the cold and warm seasons are shown in Fig. 5. The data were collected in clear air so that we knew there were no weather echoes. It is seen that insects make the distributions wider in the warm season. Clutter recognition rates based on a single parameter and the combined rules (1)-(3) are shown in Table 3. For a single polarimetric parameter, the differential phase exhibits the best performance with average recognition of about 83%. Probability of clutter detection via (1)-(3) is mostly larger than 93% for both cold and warm seasons in Oklahoma.
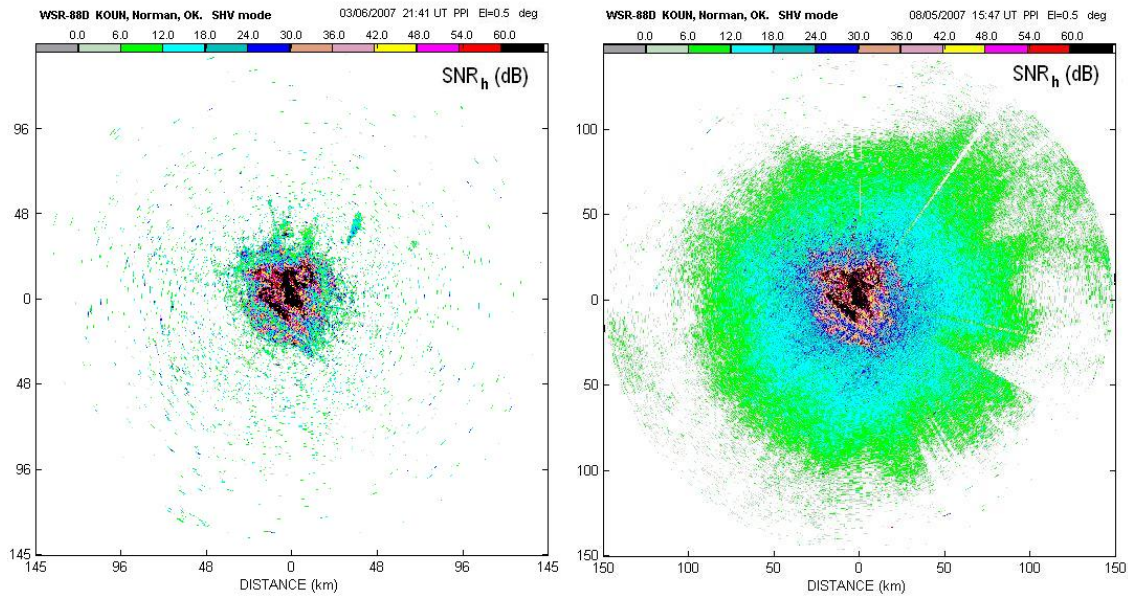


Fig.4. Clear air returns on 6 March, 2007 at 2141 UT (left panel) and 5 August 2007 at 1547 (right panel) UT. El=0.5°, M = 48. WSR-88D KOUN.

Table 3. Frequencies of clutter recognition via algorithm (1) – (3).

| Date | $Z_{DR}$ | | $\rho_{hv}$ | | $\varphi_{dp}$ | | Combined | |
|---|---|---|---|---|---|---|---|---|
| | Full spect. | 3-line spect. | Full spect. | 3-line spect. | Full spect | 3-line spect. | Full spect | 3-line spect. |
| 16 January, 2007 | 0.56 | 0.56 | 0.20 | 0.16 | 0.81 | 0.81 | 0.92 | 0.92 |
| 6 March,  2007 | 0.56 | 0.58 | 0.24 | 0.17 | 0.84 | 0.85 | 0.94 | 0.94 |
| 5 August, 2007 | 0.72 | 0.75 | 0.65 | 0.37 | 0.89 | 0.89 | 0.99 | 0.98 |
| 21 Septem., 2007 | 0.48 | 0.57 | 0.54 | 0.24 | 0.77 | 0.82 | 0.92 | 0.91 |
| 19 Decemb., 2007 | 0.54 | 0.57 | 0.30 | 0.18 | 0.84 | 0.84 | 0.93 | 0.93 |
| 17 February, 2008 | 0.59 | 0.60 | 0.28 | 0.21 | 0.83 | 0.83 | 0.94 | 0.93 |
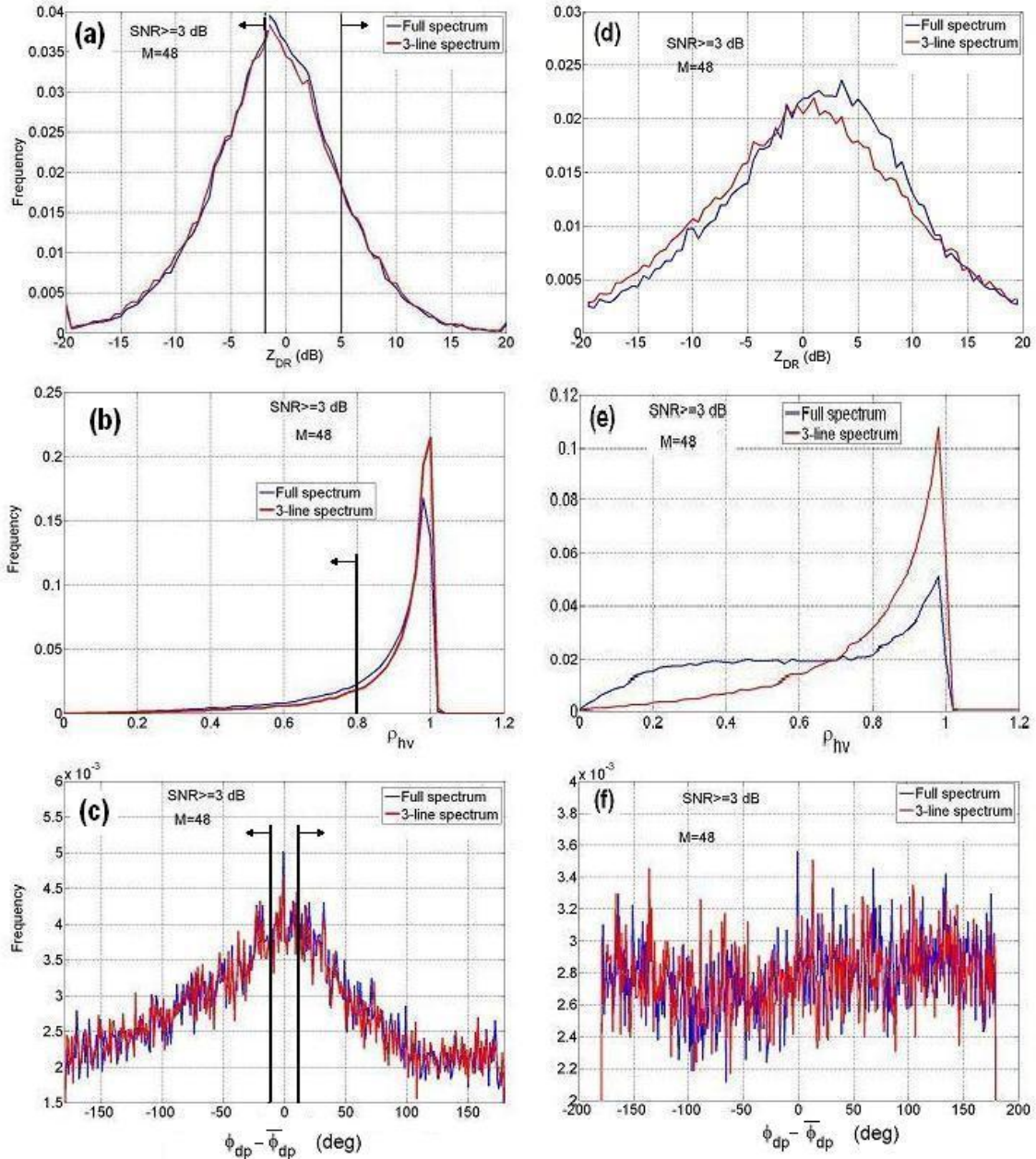
Fig.5. Distributions of the polarimetric parameters for clutter in the cold (a, b, c) and warm (d, e, f) seasons in central Oklahoma. The black vertical lines in (a, b, c) show the thresholds imposed by the algorithm (1)-(3).

*b) Weather echoes*

If a clutter recognition method is applied on an area with pure weather echoes, any recognized clutter is counted as a false alarm. To obtain the false alarm rate for algorithm (1)-(3), radar data beyond 50 km have been analyzed. At KOUN site, ground clutter is observed within 47 km under normal propagation conditions, so 50 km was

18

considered as distance beyond which echoes are fully from precipitation. In precipitation region, relative humidity is close to 100% that provides a favorable condition for anomalous propagation (AP). An example of clutter returns that are seen in precipitation echoes in the presence of AP is shown in Fig. 6a. To avoid obvious AP echoes, we have inspected echoes visually. This is not perfect because some AP echoes can be embedded in precipitation and be masked. Fig. 6b presents an example of a superposition of weather echoes and ground clutter in the absence of AP. One can see that the $\varphi_{dp}$ field has usual radial patterns and to apply rule (3), the propagation differential phase has to be obtained. The phase was calculated by averaging the measured differential phase over 2 km in range (8 range consecutive gates). No attenuation correction has been made for $Z_{DR}$ because attenuation was insignificant. Distributions of the polarimetric parameters are shown in Fig. 7 and the false alarm rates for the case are presented in Table 4. Table 4 shows that the most of false alarm rate is lower than 5%. But the rate for 15th February, 2007 case is 11%.
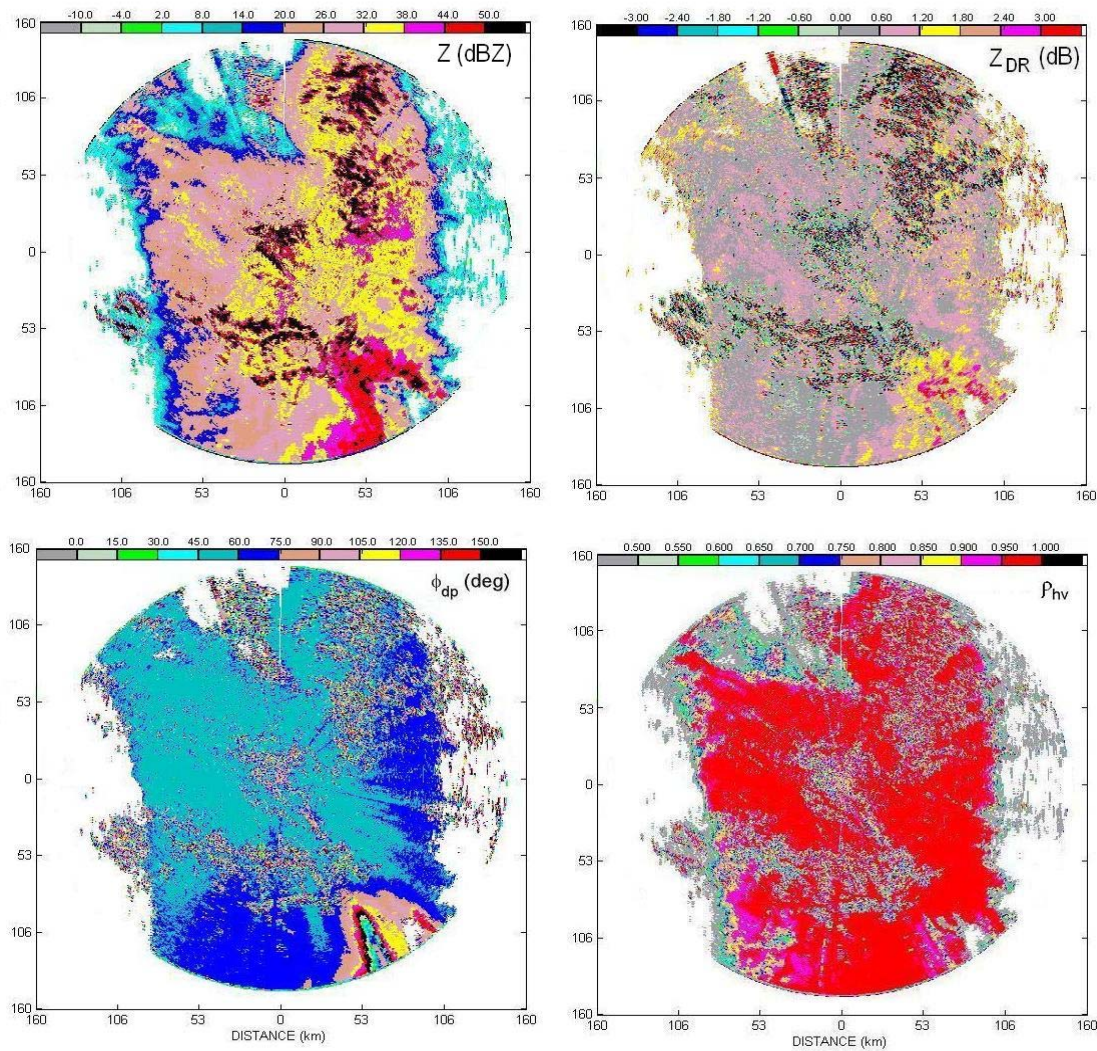


Fig.6a. Strong AP echoes in precipitation field. Z, $Z_{DR}$, $\varphi_{dp}$ and $\rho_{hv}$ on August 27, 2002 at 1051 UTC. WSR-88D KOUN.
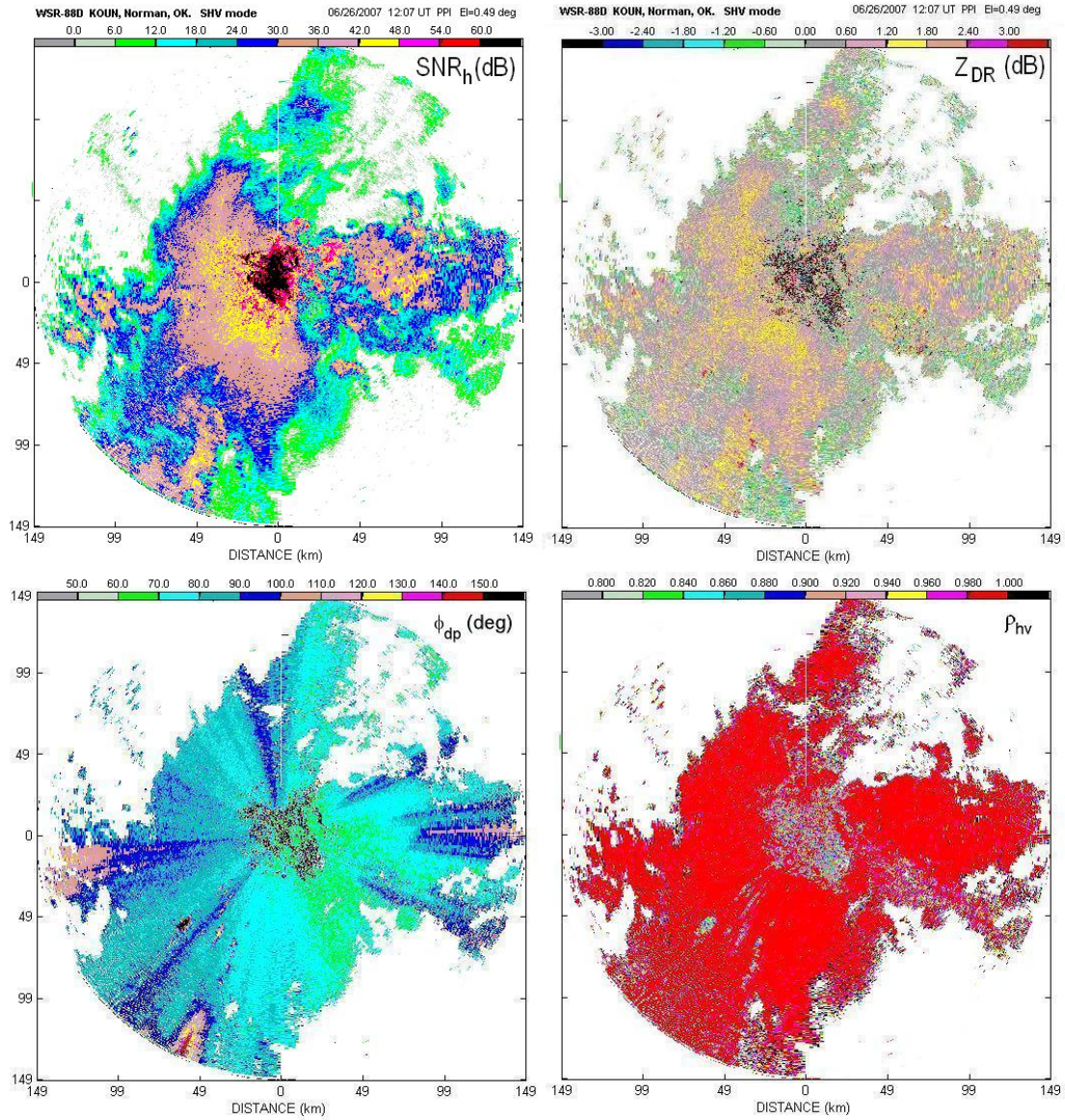
Fig.6b. Fields of SNRh, $Z_{DR}$, $\varphi_{dp}$ and $\rho_{hv}$ on June 26, 2007 at 1207. El=0.5$^o$. No AP echoes is recognized. WSR-88D KOUN.
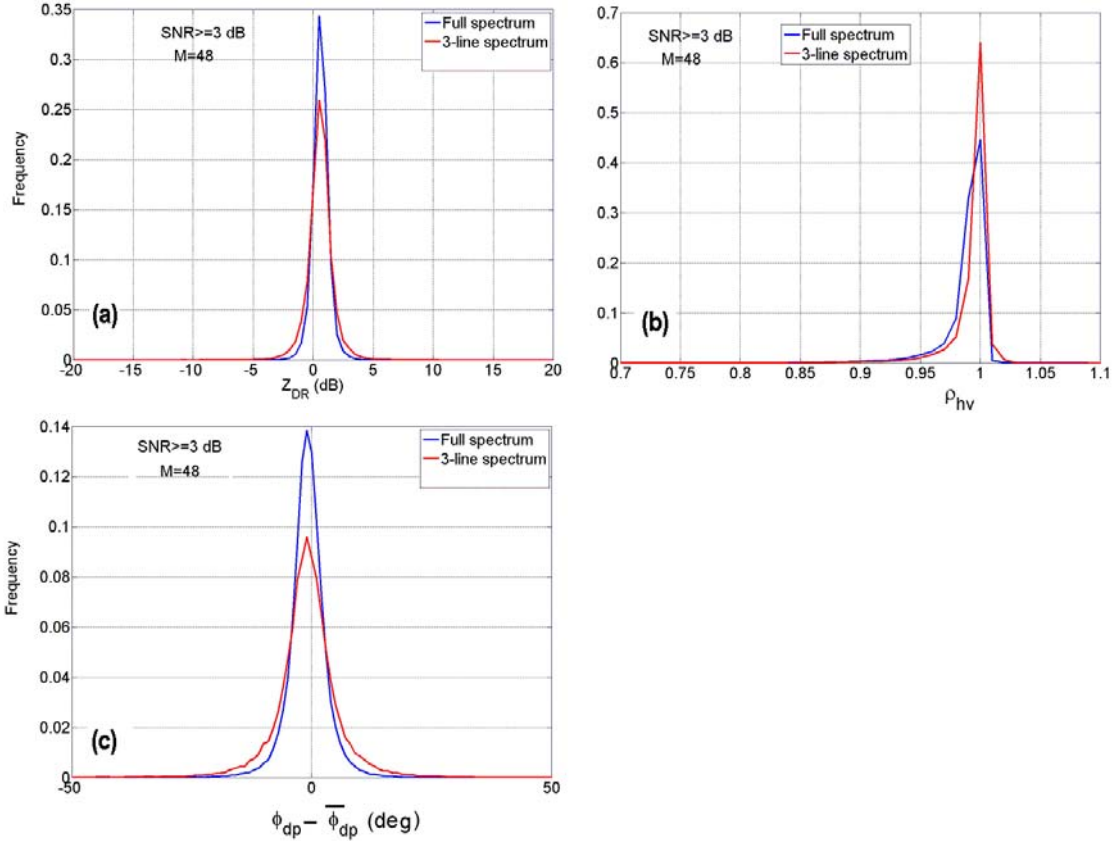
Fig.7. Distributions of $Z_{DR}$, $\rho_{hv}$ and $\varphi_{dp}$ for precipitation shown in Fig. 6b.

Table 4. False alarm rates of algorithm (1)-(3) for precipitation.

| Date | $Z_{DR}$ | | $\rho_{hv}$ | | $\varphi_{dp}$ | | Combined | |
|------|----------|--------|-------------|--------|----------------|--------|----------|--------|
| | Full spect. | 3-line spect. | Full spect. | 3-line spect. | Full spect. | 3-line spect. | Full spect | 3-line spect. |
| 12 January, 2007 | 0.001 | 0.02 | 0.001 | 0.002 | 0.001 | 0.01 | 0.003 | 0.03 |
| | 0.001 | 0.01 | 0.001 | 0.001 | 0.001 | 0.01 | 0.002 | 0.02 |
| | 0.002 | 0.02 | 0.002 | 0.003 | 0.001 | 0.01 | 0.004 | 0.02 |
| | 0.001 | 0.02 | 0.001 | 0.002 | 0.001 | 0.01 | 0.002 | 0.03 |
| | 0.001 | 0.01 | 0.001 | 0.001 | 0.001 | 0.01 | 0.002 | 0.02 |
| | 0.001 | 0.01 | 0.001 | 0.001 | 0.001 | 0.01 | 0.002 | 0.02 |
| 14 January, 2007 | 0.002 | 0.01 | 0.003 | 0.002 | 0.004 | 0.01 | 0.01 | 0.02 |
| | 0.004 | 0.02 | 0.004 | 0.004 | 0.006 | 0.02 | 0.01 | 0.04 |
| | 0.003 | 0.02 | 0.003 | 0.003 | 0.005 | 0.02 | 0.01 | 0.04 |
| | 0.002 | 0.01 | 0.002 | 0.001 | 0.005 | 0.02 | 0.01 | 0.02 |
| 15 Febr., 2007 | 0.030 | 0.05 | 0.020 | 0.003 | 0.10 | 0.14 | 0.08 | 0.11 |
| 26 June, 2007 | 0.003 | 0.02 | 0.004 | 0.007 | 0.01 | 0.05 | 0.01 | 0.04 |
| 19 August, 2007 | 0.008 | 0.03 | 0.009 | 0.012 | 0.01 | 0.05 | 0.02 | 0.07 |
| 22 Dec., 2007 | 0.004 | 0.01 | 0.004 | 0.001 | 0.003 | 0.02 | 0.01 | 0.03 |
| | 0.004 | 0.02 | 0.003 | 0.002 | 0.005 | 0.03 | 0.01 | 0.04 |

*c) Ground clutter due to anomalous propagation*

AP of electromagnetic waves results in clutter echoes at locations where there was no echo at normal refraction conditions. Examples of SNR and $Z_{DR}$ fields in the presence of AP echoes are shown in Fig. 8 (see also Fig. 6a).
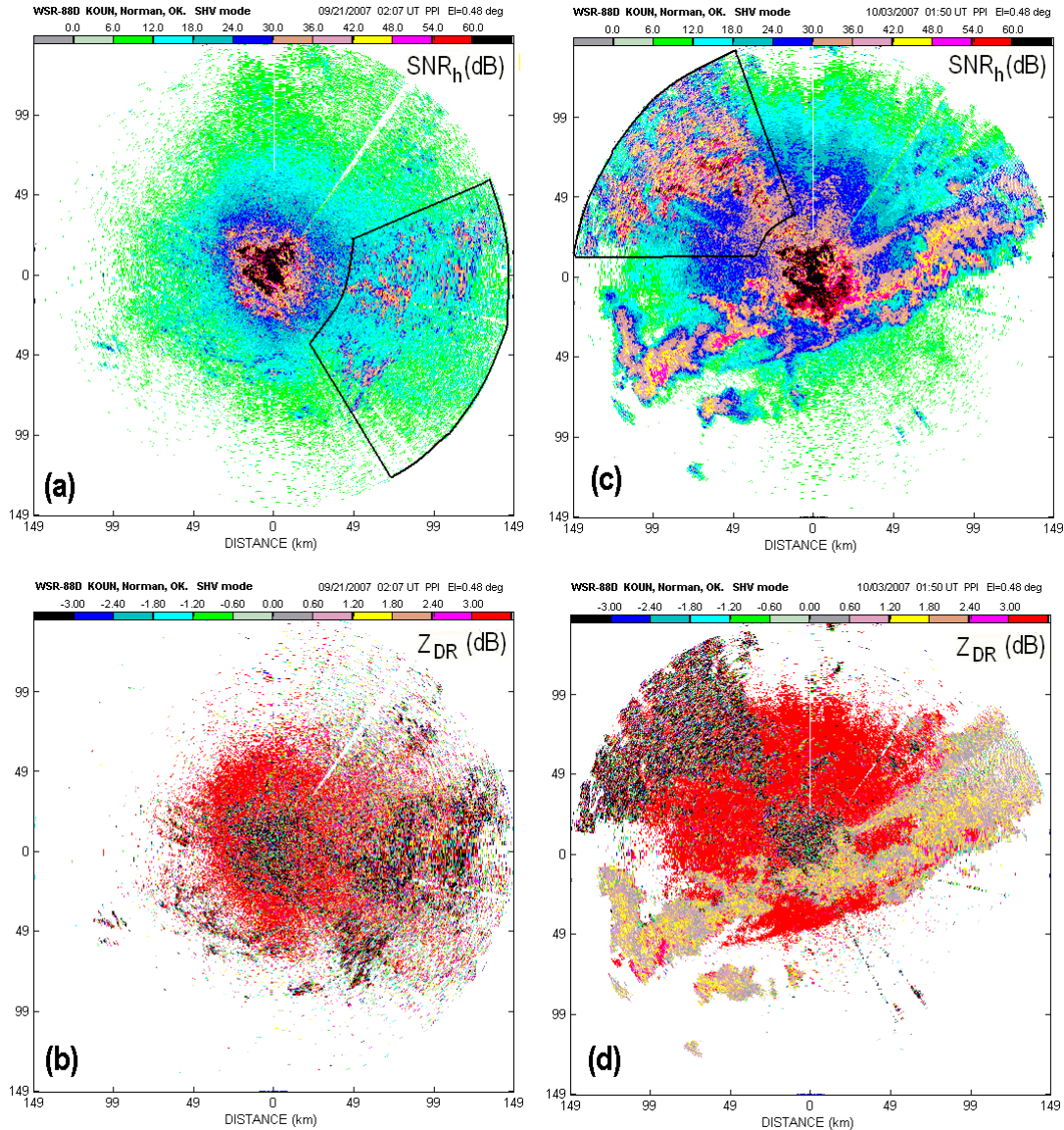


Fig. 8. AP echoes on 21 September, 2007 (a, b) and 3 October, 2007 (c, d). The fan shape sectors are the areas wherein polarimetric parameters of AP echoes have been analyzed.

The left panels in Fig. 8 contains AP in the absence of precipitation whereas AP in the right panels occurred behind the band of precipitation that moved SE. Polarimetric parameters of AP echoes have been analyzed inside areas indicated in Fig. 8 with the fan

22

shape sectors. To get rid of echoes from insects, SNR threshold of 20 dB was applied, i.e., threshold $S\tilde{N}R_{h0}$ in (4) was changed from 3 to 20 dB.

Distributions of the polarimetric variables from AP echoes are shown in Fig. 9 and probabilities of detection are in Table 5. It can be seen from Table 5 that the probability of detection (POD) of the AP echoes are about 90% which is slightly less than the POD of regular clutter shown in Table 3.
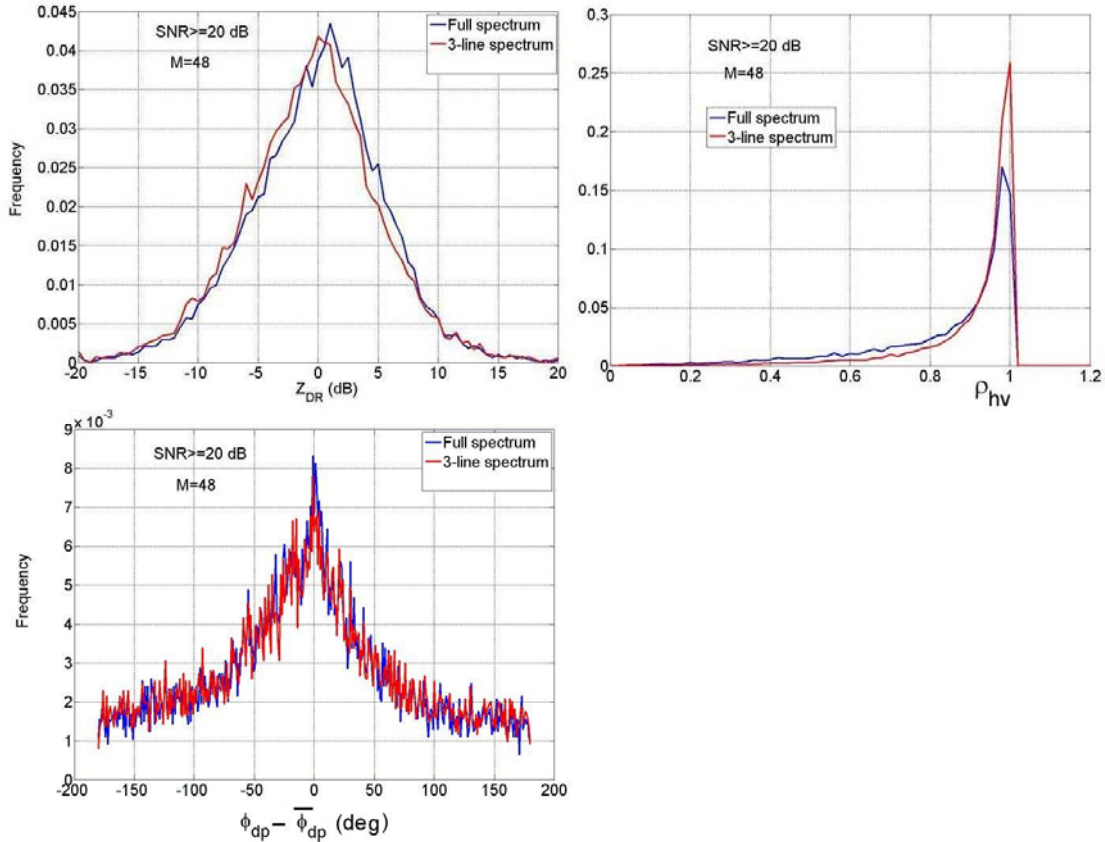


Fig.9. Distributions of $Z_{DR}$, $\rho_{hv}$, and $\varphi_{dp}$ for AP echoes on 3 October, 2007.

Table5. Frequencies of AP echoes recognition via algorithm (1) – (3).

| Date | $Z_{DR}$ | | $\rho_{hv}$ | | $\varphi_{dp}$ | | Combined | |
|---|---|---|---|---|---|---|---|---|
| | Full spect. | 3-line spect. | Full spect. | 3-line spect. | Full spect | 3-line spect. | Full spect | 3-line spect. |
| 21 Sept., 2007 | 0.53 | 0.56 | 0.16 | 0.09 | 0.81 | 0.81 | 0.91 | 0.91 |
| 3 October, 2007 | 0.53 | 0.56 | 0.26 | 0.13 | 0.77 | 0.78 | 0.89 | 0.89 |
| | 0.53 | 0.57 | 0.28 | 0.14 | 0.77 | 0.78 | 0.89 | 0.89 |

*d) Mixtures of ground clutter and weather echoes*

   Clutter recognition algorithm is meant to work in situations with superimposed precipitation and clutter. It is important to know the performance of clutter recognition algorithm (1)-(3) for a mixture of weather and clutter echoes at a gate. Combining simulated weather signal and radar observed clutter data, the frequency of clutter recognition is obtained.  Weather signals can be simulated easily using algorithm of Jenkins and Watts (1964, section 8.4.1). Simulated weather data follow the theoretical statistics of dual-polarization signals very well down to SNR = 2 dB (e.g., Melnikov and Zrnic, 2007). Simulation of clutter is more complicated because its signal consists of coherent and non coherent components (Billingsley, 2001). The coherent component is formed by stationary objects (ground itself, buildings, and big tree trunks). The non coherent component is produced by moving objects like leaves, grass, tree branches responding to the wind. Instead of simulating clutter with the two components, we used real clutter signals recorded in clear air, i.e., I and Q signal components. A mixture of weather and clutter signal at a gate has been obtained by superposing simulated I-Q components of weather with I-Q components of clutter at the KOUN site. By appropriately scaling the relative powers of weather and clutter signal we can span a range of Clutter-to-Signal Ratios (CSR). In the analysis, we could use real weather signals recorder outside regions contaminated by clutter but such signals are less versatile for the analysis. Weather signals can be simulated precisely for any polarimetric parameters and this provides more freedom in the analysis of the mix signals.

   On the KOUN, weather echoes have $\rho_{hv}$ greater than 0.95. Fig. 10 depicts the frequency of ground clutter recognition in the mixtures as a function of CSR; "weather" $\rho_{hv}$ is 0.95, the mean Doppler velocities and spectrum widths are indicated in the figure. It is seen from the figure that the clutter is recognized in the mixture with POD larger than 90% at CSR greater than 4 dB even if weather echo has zero Doppler velocity.
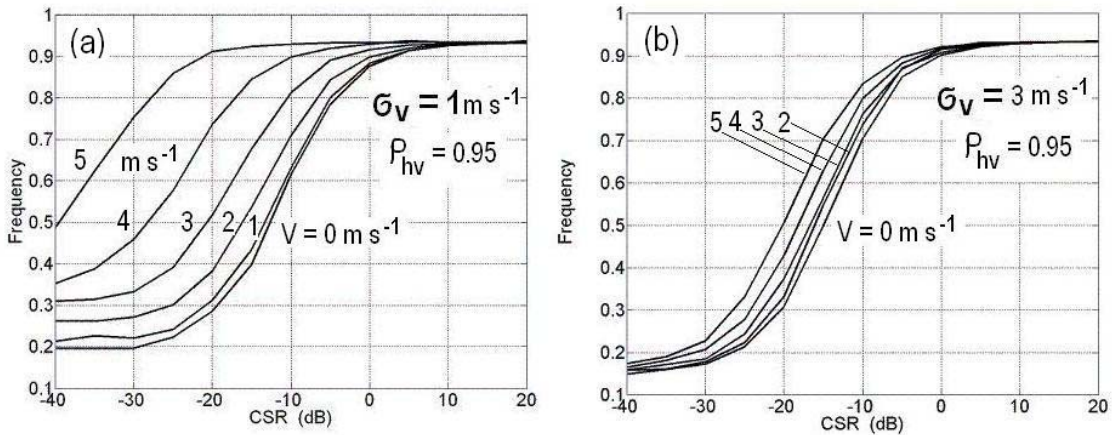


Fig.10. Frequency of clutter recognition via (1)-(3) for a mixture of clutter and weather as a function of CSR for "weather" $\rho_{hv}$ = 0.95.

In Fig. 11, recognized clutter areas are indicated with the red dots for the case shown in Fig. 6b. The weather echoes are shown with blue color. It is seen that the clutter region follows closely to clutter map recorded in clear air. There are some radials with excessive number of clutter dots in weather areas, e.g., radials at azimuths $200^o$ to $220^o$. Analysis of these echoes uncovered that such dots aroused from the second trip echoes. Therefore the algorithm (1)-(3) should be applied after range ambiguity resolution which will be done on dual-polarization WSR-88D.
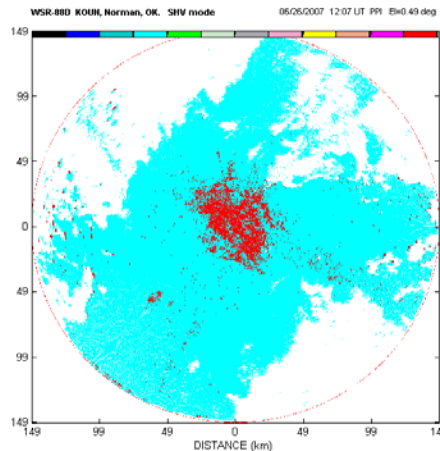


Fig.11. Recognized clutter (red dots) on the weather background (blue). June 26, 2007 at 1207. El=$0.5^o$

*e) Surveillance scans*
The lowest elevation scans of VCP11 consist of the surveillance scan (PRI=1) followed by the Doppler scan (PRI=5) at the same elevation. Both require the clutter map to activate the ground clutter filter. In the previous sections, clutter recognition was considered for the Doppler scan. That is the "instantaneous" clutter map is generated during the Doppler scan after the surveillance scan has been completed. This "instantaneous" clutter map can be applied to the subsequent surveillance scan (i.e., at the next volume scan) with a delay of about 6 min assuming that there are no major changes in the clutter location. On the other hand, the 3-line spectral method can be applied to the surveillance scan as well.

The surveillance scan is performed with PRI=1, i.e, PRF of 320 Hz which has long unambiguous range but a short Nyquist velocity interval $\pm 8.8$ m s$^{-1}$. Weather echoes with velocities around $\pm 17.6$ m s$^{-1}$ will be aliased with nearly zero Doppler velocities and such weather echoes will mask the ground clutter. This makes the Doppler scan necessary for checking the presence of aliased velocities. We consider herein a situation with no velocity aliasing. The number of samples in the surveillance mode is 17 which makes 3-line spectral interval of $2*17.6/17 = 2.1$ m s$^{-1}$, i.e., very close to $2*55.2/48 = 2.3$ m s$^{-1}$ for the Doppler mode with 48 samples. Of course, 3-line spectra at the surveillance and Doppler modes are different but closeness of the 3-line intervals makes it possible to consider algorithm (1)-(3) for the surveillance scan.

25

Algorithm (1)-(3) has been applied for the surveillance scan of VCP#11. Frequencies of true clutter recognition are shown in Table 6 and the POD is close to one for the Doppler scan (see Table 3). False alarm rates for the surveillance scan are listed in Table 8. It is seen that this rate is 9 to 14% which is noticeably larger than those for the Doppler scan (see Table 4).

Table 6. Frequencies of clutter recognition via algorithm (1) – (3) in the surveillance scan

| Date | $Z_{DR}$ | | $\rho_{hv}$ | | $\varphi_{dp}$ | | Combined | |
|---|---|---|---|---|---|---|---|---|
| | Full spect. | 3-line spect. | Full spect. | 3-line spect. | Full spect | 3-line spect. | Full spect | 3-line spect. |
| 12 Decemb., 2007 | 0.57 | 0.61 | 0.28 | 0.18 | 0.83 | 0.83 | 0.93 | 0.93 |
| 5 August, 2007 | 0.56 | 0.61 | 0.52 | 0.25 | 0.78 | 0.81 | 0.94 | 0.92 |
| 16 January, 2007 | 0.55 | 0.56 | 0.20 | 0.17 | 0.81 | 0.81 | 0.92 | 0.92 |
| 6 March, 2007 | 0.56 | 0.57 | 0.22 | 0.17 | 0.84 | 0.84 | 0.93 | 0.93 |
| 5 August, 2007 | 0.71 | 0.75 | 0.66 | 0.37 | 0.89 | 0.89 | 0.99 | 0.98 |
| 21 Sept., 2007 | 0.49 | 0.58 | 0.52 | 0.23 | 0.77 | 0.82 | 0.92 | 0.91 |

Table7. Frequencies of AP echoes recognition via algorithm (1) – (3) in the surveillance scan

| Date | $Z_{DR}$ | | $\rho_{hv}$ | | $\varphi_{dp}$ | | Combined | |
|---|---|---|---|---|---|---|---|---|
| | Full spect. | 3-line spect. | Full spect. | 3-line spect. | Full spect | 3-line spect. | Full spect | 3-line spect. |
| 21 Sept., 2007 | 0.54 | 0.56 | 0.17 | 0.09 | 0.82 | 0.81 | 0.92 | 0.91 |
| 3 October, 2007 | 0.52 | 0.55 | 0.21 | 0.10 | 0.76 | 0.77 | 0.87 | 0.87 |
| | 0.52 | 0.56 | 0.24 | 0.12 | 0.77 | 0.78 | 0.89 | 0.88 |

Table 8. False alarm rates of algorithm (1)-(3) for precipitation

| Date | $Z_{DR}$ | | $\rho_{hv}$ | | $\varphi_{dp}$ | | Combined | |
|---|---|---|---|---|---|---|---|---|
| | Full spect. | 3-line spect. | Full spect. | 3-line spect. | Full spect. | 3-line spect. | Full spect | 3-line spect. |
| 29 June,2007 | 0.04 | 0.07 | 0.04 | 0.02 | 0.04 | 0.08 | 0.08 | 0.13 |
| 3 March, 2008 | 0.004 | 0.04 | 0.004 | 0.01 | 0.006 | 0.05 | 0.01 | 0.09 |
| | 0.01 | 0.04 | 0.004 | 0.01 | 0.006 | 0.05 | 0.01 | 0.09 |
| 6 March, 2008 | 0.01 | 0.04 | 0.005 | 0.002 | 0.02 | 0.06 | 0.03 | 0.09 |
| | 0.01 | 0.04 | 0.005 | 0.001 | 0.02 | 0.06 | 0.03 | 0.10 |
| 18 March, 2008 | 0.008 | 0.06 | 0.02 | 0.04 | 0.01 | 0.07 | 0.03 | 0.14 |
| | 0.007 | 0.06 | 0.02 | 0.04 | 0.01 | 0.07 | 0.03 | 0.14 |

**II.4. Clutter suppression**

The main purpose of this report is studying of ground clutter recognition, i.e., the first step of clutter mitigation. The second step is ground clutter suppression which is done on the legacy system with the GMAP filter. The GMAP filter provides clutter suppression of 30 to 50 dB (Ice et al., 2004). Distributions of the clutter powers in the two polarimetric channels at the KOUN site are shown in Fig. 12. It is seen that the 3-line spectrum can have very strong SNR exceeding 100 dB. It means that clutter filtering has to be done in a wide range of CSRs of about 100 dB. There is no technique that effectively filters clutter over such a wide interval. One of the best existing techniques for a single channel radars is the GMAP filter with clutter suppression of 30 to 50 dB.

To study the performance of the GMAP filter on dual-polarized radar, we applied the filter in the H- and V-channels independently. The resulting polarimetric fields are displayed in Fig. 13. It is seen that the filter suppresses some echoes with the Doppler velocities close to zero as it should do. It is also seen that the filter destroys $Z_{DR}$ and $\rho_{hv}$ fields (it affects also the differential phase field that is not shown in Fig. 13).

Then we applied clutter recognition algorithm (1)-(3) and used GMAP filter in the gates with recognized clutter. The GMAP filter was applied not independently in the H- and V-channels. Firstly, the GMAP filter was used in the H-channel alone to determine the spectral coefficients belonging to clutter. Then those spectral coefficients were used to suppress clutter in both H- and V-channels. The resulting fields are shown in Fig. 14. Comparing with Fig. 13, one can see that the above approach produces more realistic polarimetric fields.
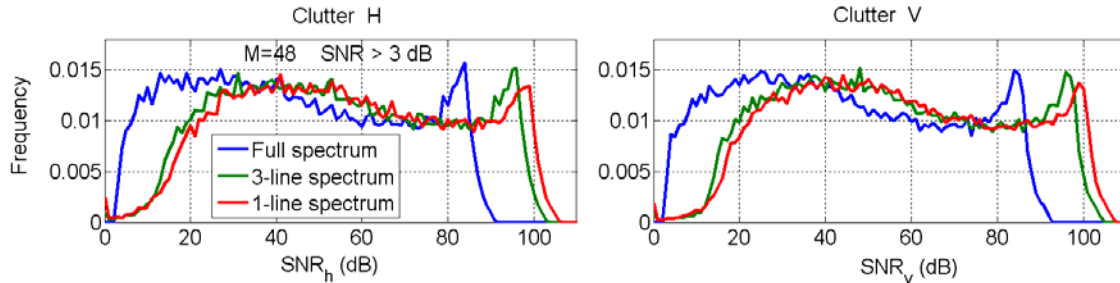


Fig.12. Distributions of SNR$_h$ and SNR$_v$ for ground clutter on 6 March, 2007. The 1-line spectrum is the central spectral line, i.e., the DC component.
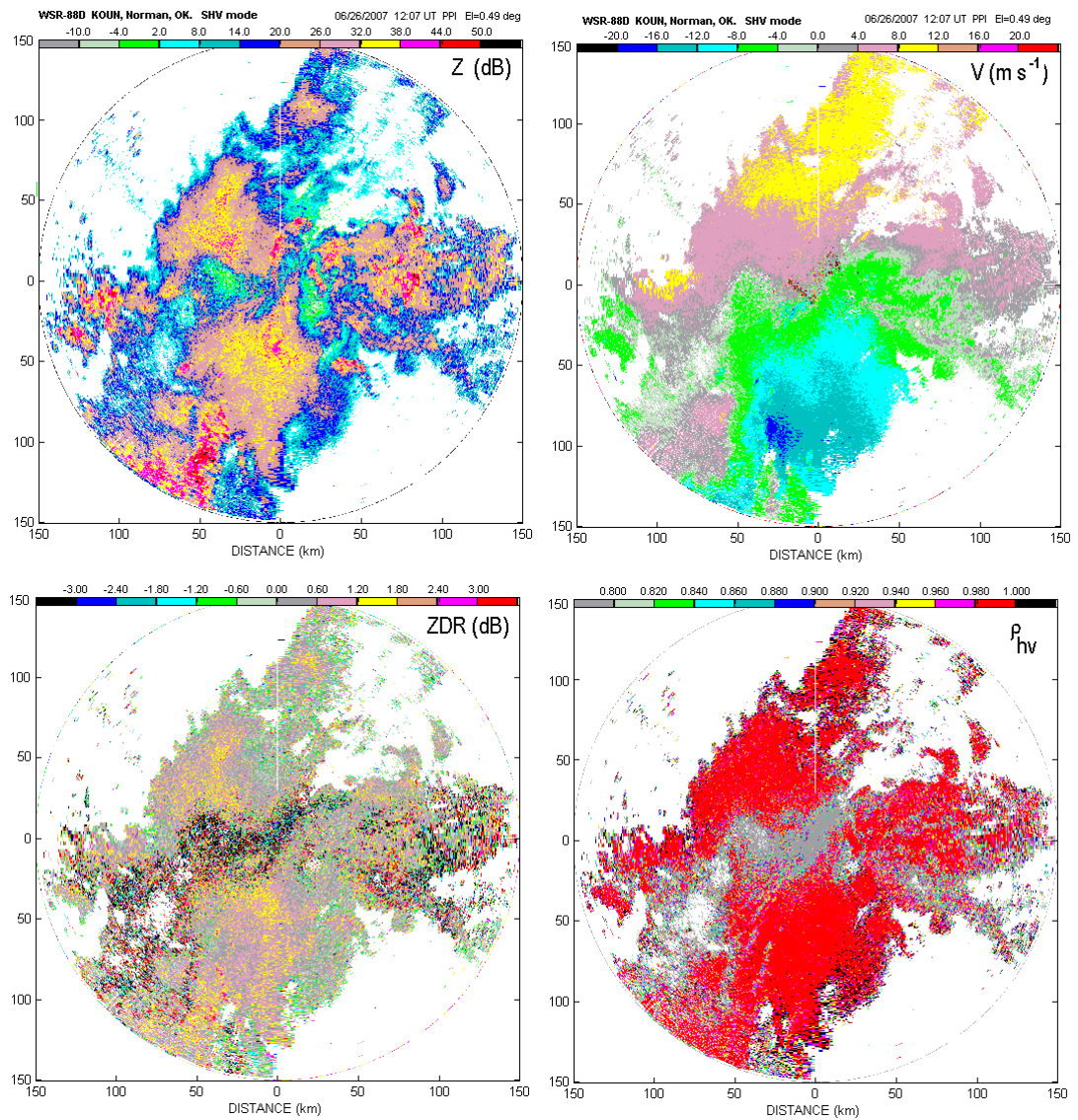
Fig.13. Fields of the polarimetric variables and Doppler velocity after applying GMAP independently to both channels. Filter is applied everywhere.
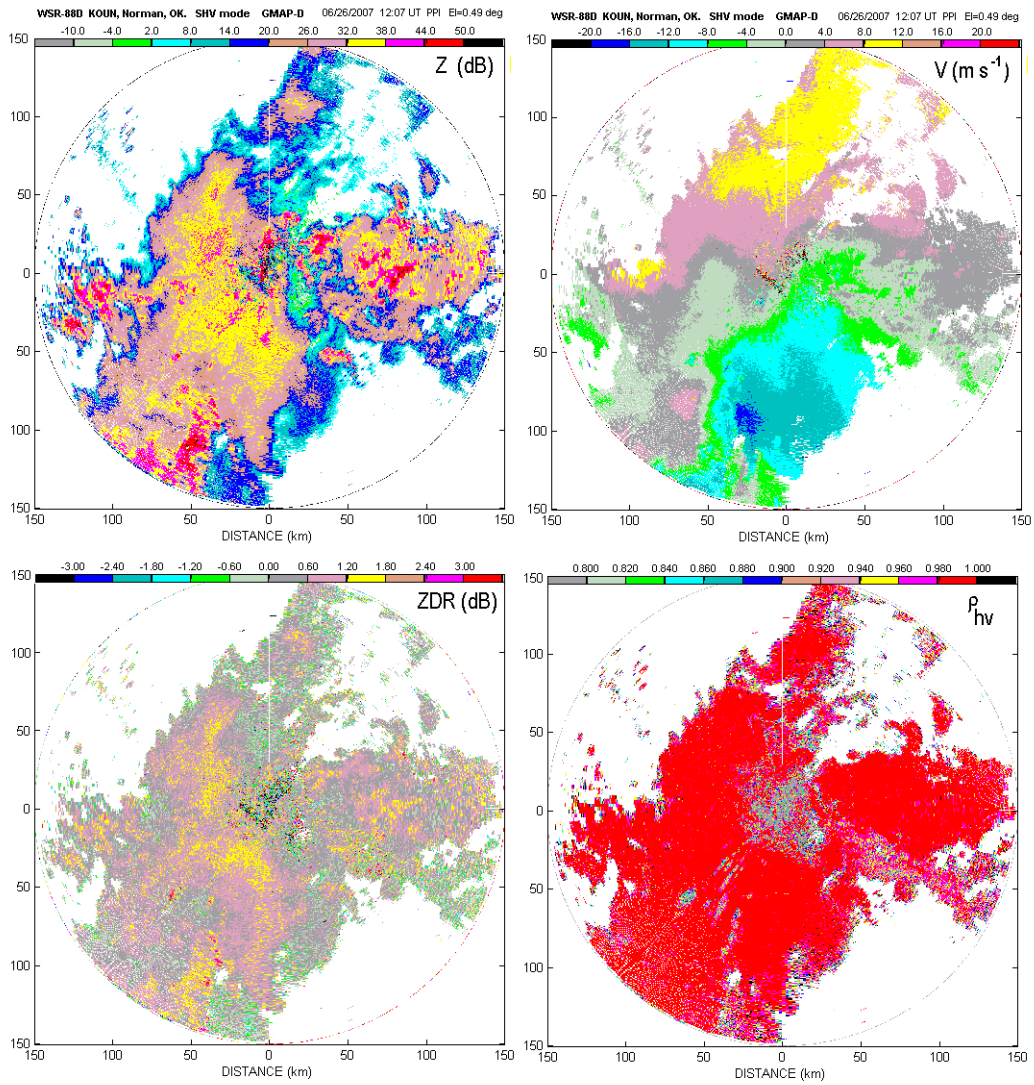
Fig.14. Same as in Fig. 13 except the suppressed coefficients are determined by GMAP in the H channel. Then these coefficients are removed from both the H and the V channel at range locations where the clutter has been indentified with 3-line algorithm (1)-(3).

**II.5. Conclusions**

The algorithm (1)-(3) of clutter recognition based on polarimetric variables obtained from three central lines of the Doppler spectrum has been applied to the surveillance and Doppler modes of the WSR-88D with relatively small numbers of samples 17 and 48.

In the Doppler mode, the algorithm demonstrates about 93% of average recognition rate and average false alarm rate of 4%. Recognition rate of echoes due to anomalous propagation is about 90%. For a mixture of weather and clutter, clutter is recognized with the POD larger than 90% at clutter-to-signal-ratio greater than 4 dB even if weather echo has zero Doppler velocity (for the spectrum width smaller than 3 m s$^{-1}$). To maintain the accuracy of clutter recognition, the following data preprocessing procedures should be executed before clutter recognition: 1) remove echoes from the second and third trips, 2) correct the $Z_{DR}$ bias caused by attenuation, and 3) locate the bright band.

In the surveillance mode, the method demonstrates average POD of about 93% i.e., the same as in the Doppler mode, but the false alarm rate is about 12%. Recognition of echoes due to anomalous propagation has average POD of about 88% which is slightly less than the one in the Doppler mode.

Changing the polarimetric thresholds can improve the clutter recognition rate to some degree by narrowing the threshold intervals indicated in (1)-(3). The lower $Z_{DR}$ threshold parameters, i.e., $\widetilde{Z}_{DR2}$ = -2 dB, can be raised up using correction of differential reflectivity for differential attenuation. Used $\rho_{hv}$ threshold at 0.8 defends the algorithm against low level bright bands which are observed in central Oklahoma only in the cold seasons. The removal of the second and third trip echoes will also increase the probability of ground clutter recognition. Thus, with further refinement it is worthy considering the generation of an "instantaneous clutter maps" using the 3-line method. Relative simplicity and signal processing at single range gate are in its favor. Furthermore, clutter can be removed immediately after its recognition with minimal additional computations. The algorithm also prevents the removal of weather signals in some situations with zero Doppler velocity.

### Appendix to section II

The following power comparison can be incorporated into the 3-line method to improve its computational performance. It is obvious that if the weather power is much stronger than the clutter power, the echo is "weather like" and there is no need for any clutter recognition algorithm even if the clutter power is not weak. In this appendix, we find a CSR at which no ground clutter recognition or filtering is needed, i.e., echo can be considered as "weather like".

At a given range gate, the spectrum is considered "weather like" if the following relative power, $R_p$,

$$R_p = 10\log(\frac{\widetilde{P}}{P}) \le -30 \quad dB. \tag{A1}$$

for the both H- and V-channels. In other words, if the signal power of the 3-line spectrum is at least 30 dB weaker than the total power, the clutter contribution can be ignored. Clutter signals never pass inequality (A1) because the 3-line spectrum contains almost all its power.

Consider application of (A1) for a mixture of weather and clutter signals. Let indexes 'c' and 'w' stand for clutter and weather returns. If (A1) is satisfied, $Z_{DR}$ is

$$Z_{DR} = 10\log\frac{S_{hw} + S_{hc}}{S_{vw} + S_{vc}} = Z_{DRw} + 10\log\left(\frac{1 + S_{hc}/S_{hw}}{1 + S_{vc}/S_{vw}}\right) \approx Z_{DRw} + \frac{1}{\ln 10}\left(\frac{S_{hc}}{S_{hw}} - \frac{S_{vc}}{S_{vw}}\right).$$

Where $S$ stands for signal power, i.e., the returned power minus noise power. We see that $Z_{DR}$ is biased but the bias is smaller than $10^{-3}$ dB and it can be neglected.

Now consider $\rho_{hv}$. let $R$ be the module of the correlation function of the signal so that $R = (S_h S_v)^{1/2}\rho_{hv}$. We also define $R_w = (S_{hw}S_{vw})^{1/2}\rho_{hvw}$ and $R_c = (S_{hc}S_{vc})^{1/2}\rho_{hvc}$ for the weather and clutter contributions separately. For mixture of weather and clutter, $R = R_w + R_c$. Coefficient $\rho_{hv}$ has the largest bias if clutter is uncorrelated, i.e., $\rho_{hvc} = 0$. In this case,

$$\rho_{hv} = \frac{R_w}{[(S_{hw} + S_{hc})(S_{vw} + S_{vc})]^{1/2}} = \rho_{hvw}\frac{1}{[(1 + S_{hc}/S_{hw})(1 + S_{vc}/S_{vw})]^{1/2}} \approx \rho_{hvw}(1 - \frac{1}{2}\frac{S_{hc}}{S_{hw}} - \frac{1}{2}\frac{S_{vc}}{S_{vw}}).$$

It follows from the latter that if (A1) is fulfilled, the bias of $\rho_{hv}$ is less than $2\times10^{-3}$ and can be neglected.

For $\varphi_{dp}$ measurements, let $R$ be the signal complex correlation function so that $R = (S_h S_v)^{1/2}\rho_{hv}\exp(j\varphi_{dp})$ and for a mixture of weather and clutter returns, we write $R = R_w + R_c = (S_{hw}S_{vw})^{1/2}\rho_{hvw}\exp(j\varphi_{dpw}) + (S_{hc}S_{vc})^{1/2}\rho_{hvc}\exp(j\varphi_{dpc})$. Tangent of the measured differential phase is

$$\tan(\varphi_{dp}) = \frac{\sin(\varphi_{dpw}) + x\sin(\varphi_{dpc})}{\cos(\varphi_{dpw}) + x\cos(\varphi_{dpc})}, \qquad x = \frac{(S_{hc}S_{vc})^{1/2}\rho_{hvc}}{(S_{hw}S_{vw})^{1/2}\rho_{hvw}} \ll 1.$$

Consider two opposite cases, $\varphi_{dpw} = 0$ and $\varphi_{dpw} = 90^{\circ}$. In the first case,

$$\tan(\varphi_{dp}) = \frac{x\sin(\varphi_{dpc})}{1 + x\cos(\varphi_{dpc})} \approx x\sin(\varphi_{dpc}) \leq 0.11^{o}.$$

In the second case,

$$\tan(\varphi_{dp}) = \frac{1 + x\sin(\varphi_{dpc})}{x\cos(\varphi_{dpc})} \approx \frac{1}{x\cos(\varphi_{dpc})} > 10^3,$$

$$\varphi_{dp} \approx 90^{\circ} - 0.06^{\circ}.$$

We see that in both of these cases, the $\varphi_{dp}$ bias is small and therefore it is small for any case if (A1) is satisfied. Considering $\varphi_{dp}$ measurements we assumed positive $\cos(\varphi_{dpc})$. It is not difficult to consider negative $\cos(\varphi_{dpc})$ and come to the same conclusion. Thus we conclude that the biases of the polarimetric variables are small if (A1) is satisfied and signal can be considered weather-like regardless of the presence of clutter.

**References**

Berenguer M., D. Sempre-Torres, C. Corral, and R. Sanches-Diezma, 2006: A fuzzy logic technique for identifying nonprecipitating echoes in radar scans. *J. Atmos. Ocean. Technol.*, **23**, 1157-1179.

Billingsley, J.B., 2001: *Low angle radar land clutter*. William Andrew Publishing, 703 pp.

Dixon, M., C. Kessinger, and J. Hubbert, 2006: Echo classification within the spectral domain to discriminate ground clutter from meteorological targets. IIPS, P9.6.

Doviak, R. J. and D. S. Zrnic, 2006: *Doppler radar and weather observations*, 3$^{rd}$ ed., Academic Press, 562 pp.

Ellis, S., C. Kessinger, J. VanAndel, M. Dixon, and J. Hubbert, 2003: Enhancements in clutter/precipitation discrimination for the WSR-88D. IIPS 19, P2.9.

Gourley, J.J., P.Tabary, and J. P. du Chatelet, 2007: A fuzzy logic algorithm for the separation of precipitating from nonprecipitating echoes using polarimetric radar observations. *J.Atmos. Ocean. Technol.*, **24**, 1439-1451.

Ice, R.L., R.D.Rhoton, D.S. Saxion, N.K. Patel, D.A. Sirmans, D.A. Warde, D.L. Rachel, and R.G. Fehlen, 2004: Evaluation of the WSR-88D ORDA system signal processing. 20$^{th}$ IIPS.

Kessinger C., J. VanAndel, S. Ellis, G. Meymaris, 2003:The radar echo classifier: a fuzzy logic algorithm for the WSR-88D. 3$^{rd}$ Conf. Artif. Intell. Applic to Envir. Sci., AMS, 9-13.

Saffle, R. E., G. S. Cate, and M. Istok, 2007: NEXRAD Product Improvement—Update 2007. *23 Conf. on IIPS, Amer. Meteorol. Soc*., San Antonio, TX, paper 5B.1.

Siggia, A.D., and R.Passarelli Jr., 2004: Gaussian model adaptive processing (GMAP) for improved ground clutter cancellation and moment calculation. 3rd European Conf. Radar Meteorol. Hydrol.(ERAD), 67-73.

Steiner, M, and J.A. Smith, 2002: Use of three–dimensional reflectivity structure for automated detection and removal of nonprecipitating echoes in radar data. *J.Atmos. Ocean. Technol.*, **19**, 673-686

Yo-Han Cho, GyuWon Lee, Kyung-Eak Kim, and I. Zawadzki, 2006: Identification and removal of groung echoes and anomalous propagation using the characteristics of radar echoes. *J. Atmos. Ocean. Technol.*, **23**, 1206-1222.

Zrnic, D.S., A. Ryzhkov, J. Straka, Y. Liu, and J. Vivekanandan, 2001: Testing a procedure for automatic classification of hydrometeor types. *J. Atmos. Ocean. Technol.*, **18**, 892-913.

Zrnic, D.S., V.M. Melnikov, and A. V. Ryzhkov, 2006: Correlation coefficients between horizontally and vertically polarized returns from ground clutter. *J. Atmos. Ocean. Technol.*, **23**, 381-394.